One-dimensional fuzzy dark matter models: Structure growth and asymptotic dynamics

Tim Zimmermann[,1,*] Nico Schwersenz,[1,†] Massimo Pietroni[,2,3,‡] and Sandro Wimberger[2,3,§]

[1]*Institut für Theoretische Physik, Philosophenweg 16, 69120 Heidelberg, Germany*
[2]*Dipartimento di Scienze Matematiche, Fisiche e Informatiche, Universitá di Parma,*
Campus Universitario, Parco Area delle Scienze n. 7/a, 43124 Parma, Italy
[3]*INFN, Sezione di Milano Bicocca, Gruppo Collegato di Parma, 43124 Parma, Italy*

This paper investigates the feasibility of simulating fuzzy dark matter (FDM) with a reduced number of spatial dimensions. Our aim is to set up a realistic, yet numerically inexpensive, toy model in $(1+1)$-dimensional space time, that—under well controlled system conditions—is capable of realizing important aspects of the full-fledged $(3+1)$-FDM phenomenology by means of one-dimensional analogues. Based on the coupled, nonlinear and nonlocal $(3+1)$-Schrödinger-Poisson equation under periodic boundary conditions, we derive two distinct one-dimensional models that differ in their transversal matter distribution and consequently in their nonlocal interaction along the single dimension of interest. We show that these discrepancies change the relaxation process of initial states as well as the asymptotic, i.e., thermalized and virialized, equilibrium state. Our investigation includes the dynamical evolution of artificial initial conditions for nonexpanding space, as well as cosmological initial conditions in expanding space. The findings of this work are relevant for the interpretation of numerical simulation data modeling nonrelativistic fuzzy cold dark matter in reduced dimensions, in the quest for testing such models and for possible laboratory implementations of them.

I. INTRODUCTION

Nonlinear Schrödinger equations are ubiquitous in physics. Let us just think of interacting many-body problems in nonrelativistic condensed-matter theory that are reduced to a mean-field approximation that usually ends up in a nonlinear effective Schrödinger equation; see e.g., [1–4]. A specific form of a such a nonlinear equation is the Schrödinger-Poisson, also known as Schrödinger-Newton equation, describing a scalar massive quantum particle in its own gravitational field. It finds many applications, e.g., in nonlinear optics [5–8], decoherence theory [9], and, of course, in cosmology [10], whenever a nonrelativistic description of the particle suffices. Reference [11] presents a recent review on the subject.

Here, we are interested in the Schrödinger-Poisson (SP) equation as an alternative dark matter model to the established cold dark matter (CDM) paradigm. Hu *et al.* [12] dubbed the matter so described fuzzy cold dark matter, or simply fuzzy dark matter (FDM), a notion that we will follow throughout the paper.

[*]zimmermann@thphys.uni-heidelberg.de
[†]schwersenz@thphys.uni-heidelberg.de
[‡]massimo.pietroni@unipr.it
[§]sandromarcel.wimberger@unipr.it

The most compelling feature of FDM obeying SP in four-dimensional $(3+1)$ space-time is its distinct behavior on large and small spatial scales: Assuming a dark matter particle mass of $m \approx 10^{-22}$ eV—canonical for FDM—cosmic structure growth under FDM is in accordance with CDM on supergalactic scales, e.g., identical matter power evolution or halo densities [13], subgalactic scales are influenced by quantum mechanical effects. In particular, one expects the existence of a solitonic state, with a flat, high-density core region, that is roughly speaking obtained from a balance of quantum pressure and gravity [12]. Structure smaller than the solitonic core is suppressed, or smoothed out, by the uncertainty principle. Thus, FDM may provide a natural solution to the small scale crisis of CDM [14], and in particular its cusp-core problem, [15–17], without the need of adding sophisticated baryonic feedback processes. From a fundamental physics point of view, SP simulations could predict the mass scales of the bosonic particles possibly constituting dark matter, of course in comparison with and constrained by experimental observation data [18–21]. We note in passing that SP simulations may also be interpreted as an alternative sampling approach of the CDM phase space evolution that may be controlled by the phase space resolution $\hbar/m$; see e.g., [22–26].

Numerical considerations of the $(3+1)$-SP equation, see e.g., [13,17,27–29], identify the soliton state as a dynamical

attractor in the time evolution of FDM. More precisely, overdense regions collapse under their self-gravity and during this process radiate away excess matter. The result of this process, sometimes dubbed gravitational cooling, [30], is a relaxed quantum matter distribution in which a solitonic core is immersed in a "sea of fluctuations." The latter follows a power-law decay, with a radial profile, known as Navarro–Frenk–White (NFW) profile, predicted in corresponding many-body simulations of CDM [31] to scale as $\rho \propto r^{-3}$ at large radii.

This paper addresses the question whether the time-asymptotic behavior just described, or at least a similar scenario thereof, were recovered if only 1 spatial degree of freedom is available. In other words, can we derive a one-dimensional, yet sufficiently realistic, toy model that realizes one-dimensional analogues of the $(3 + 1)$-FDM structure formation, and in particular the mentioned solitonic core and its role as dynamical attractors? This includes, both the evolution to and the possible reaching of the asymptotic state, hence the relaxation process itself as well as its final product. Are the relaxation mechanisms in one-dimensional FDM the same as for 3D FDM; i.e., is there a one-dimensional analogue of gravitational cooling? What are suitable astrophysical, quantum mechanical or statistical measures to judge if the asymptotic state has been reached? These questions have several motivations. Firstly, it is *a priori* not clear whether a model with reduced dimension will lead to the same evolution as the full-fledged three-dimensional one, simply because assumptions on the matter configuration in the transversal dimensions must be made and, in higher dimensions, interdimensional coupling and redistribution of mass is, in principle, possible due to the nonseparable nonlinearity [32]. Secondly, it is needless to say that models with reduced dimensions lend themselves to much more detailed investigations even on relatively long spatial and temporal scales. Reliable high-precision numerical simulations are simply more efficient in one than in higher dimensions. Consequently, larger patches of the system's parameter space can be covered with manageable resources. The reduced numerical complexity also allows us to generate large ensembles of simulations once a, in some sense optimal, parameter set was identified, thereby reducing statistical uncertainties without the need to invoke assumptions like ergodicity. Obviously, both aspects, i.e., parameter space coverage and statistical reliability, are vital for comparison with observational data.

The way of the reduction of dimensionality will certainly be important. Anticipating our results, we will see that the relaxation process in the evolution as well as in the finally reached states do depend strongly on how matter is organized in the transversal dimensions. The usual approach of assuming a uniform matter distribution in the transverse dimension, and hence in practice just forgetting about the other degrees of freedom, does not

yield a correspondence with the $(3 + 1)$-FDM predictions. This motivated our second approach in which we confine the transverse degrees of freedom. Then, most of these predictions are actually seen in the reduced one-dimensional model as well. Our findings are based on a relative simple but highly flexible, efficient and precise numerical method to integrate both dimensionality-reduced SP equations. This allows us access to long temporal evolutions in a constant as well as in an expanding universe.

The paper is organized as follows: the next section reviews the theory of FDM based on the SP equation. We discuss therein the importance of the reduction to $(1 + 1)$ (space + time) dimensions, and we compare, in particular, the two ways of doing this: first, we assume a uniform extension in the transverse directions, then secondly a cigar-shaped transversal confinement. Section III gives details on our numerical methods and its properties and quality. Section IV reports our central results and compares the outcome of different numerical simulations of the two versions of reduction to $(1 + 1)$. The last section, Sec. V, concludes the paper with a short outlook on open questions and future work.

II. THEORETICAL BACKGROUND

Point of departure for our discussion is the dynamics of fuzzy dark matter (FDM) in $(3 + 1)$ dimensions. To this end, we introduce its governing equation, comment on its origin and mention different interpretations of the FDM model. After a quick review of the hydrodynamic formalism in the linear evolution regime, the remainder of this section is devoted to the problem of dimensional reduction. More precisely, two competing one-dimensional FDM representations are derived, and their physical discrepancies and similarities are highlighted. This includes an in-depth discussion on the preparation and properties of the $(1 + 1)$-FDM ground state. We close this theory section by commenting on possible relaxation mechanisms and introduce suitable metrics for $(1 + 1)$-FDM to quantify if an equilibrated system state is reached.

A. Fuzzy dark matter in $(3 + 1)$ dimensions

1. Governing equations

For the sake of simplicity, envision a universe with negligible contribution of baryonic matter and radiation towards the cosmic energy budget. Furthermore, let dark energy be given by means of a time independent energy density $\rho_\Lambda c^2$. Under these assumptions only dark matter dynamics plays a nontrivial role.

Starting from a massive, minimally coupled, scalar field, one derives, e.g., [33], the $(3 + 1)$-Schrödinger-Poisson (SP) equation as governing equation of $(3 + 1)$-FDM applicable in the nonrelativistic limit $c \to \infty$,

$$i\hbar\partial_t\Psi = \left[-\frac{\hbar^2}{2ma^2}\triangle + m\Phi\right]\Psi,$$

$$\triangle\Phi = \frac{4\pi G}{a}(|\Psi|^2 - \rho_m), \qquad x \in \Omega, \qquad (1)$$

with $\Omega = \Omega_1 \times \Omega_2 \times \Omega_3 \subset \mathbb{R}^3$ and $\Omega_i = [0, L_i)$. Here, Ψ denotes the nonrelativistic FDM field coupled to its own gravitational potential Φ. Fields are evaluated at comoving position $\boldsymbol{x} = (x_1, x_2, x_3)^\intercal$ and cosmic time t. Densities are measured with respect to a comoving volume, so that ρ_m coincides with the present day total matter density. m denotes the FDM particle mass. In accordance with our initial assumptions on the composition of the cosmic energy budget, the scale factor $a(t)$ obeys the flat space, radiation free Friedmann equation,

$$\left(\frac{\dot{a}}{a}\right)^2 = \frac{8\pi G}{3}(\rho_m a^{-3} + \rho_\Lambda).$$

G is Newton's constant.

Analyzing the asymptotic behavior of the energy momentum tensor associated with Ψ suggests the identification,

$$|\Psi(\boldsymbol{x}, t)|^2 \overset{!}{=} \rho_m(\boldsymbol{x}, t) \equiv \rho_m + \delta\rho(\boldsymbol{x}, t), \qquad (2)$$

i.e., the scalar field encapsulated both the time-independent background density ρ_m and deviations from it, $\delta\rho(\boldsymbol{x}, t)$. Since density deviations vanish upon averaging over Ω, Eq. (2) translates directly into a normalization condition on Ψ,

$$\rho_m = \frac{1}{L_1 L_2 L_3} \int_\Omega d^3x |\Psi(\boldsymbol{x}, t)|^2 = \text{const.} \qquad (3)$$

We emphasize Eq. (3) is a physically relevant constraint as Eq. (1) is *nonlinear*. Therefore changing the normalization of Ψ will lead to a different time evolution.

Equation (1) still requires suitable boundary conditions. The natural choice for modeling an infinite system is to impose the following periodic boundary conditions:

$$\partial_{x_i}^m\Psi(0, x_j) = \partial_{x_i}^m\Psi(L_i, x_j), \qquad m \in \{0, 1\},$$
$$\partial_{x_i}^m\Phi(0, x_j) = \partial_{x_i}^m\Phi(L_i, x_j), \qquad i \in \{1, 2, 3\},$$
$$j \in \{1, 2, 3\} \setminus \{i\}. \qquad (4)$$

2. Interpretations of (3 + 1)-Schrödinger-Poisson

It is instructive to shed some light onto the physical character of the nonrelativistic scalar Ψ. Although Eq. (1) has the mathematical structure of Schrödinger's equation, there is *a priori* nothing quantum mechanical about the problem. Hence, the least arcane way to interpret Eq. (1) is in a literal sense, i.e., as the Euler-Lagrange equation of a classical Lagrangian and $\hbar$ as a constant with dimensions of an action but with a numerical value not constrained to Planck's constant.

That said, there is significant value in finding (formal) correspondences between $(3 + 1)$-SP and other, potentially noncosmological, theories as it enlarges the number of available tools with which FDM can be analyzed.

Cosmic Bose-Einstein condensate.—In fact, Eq. (1) can also be identified with the evolution equation of a self-gravitating Bose-Einstein condensate with negligible local self-interaction and Ψ as the condensate *wave function*. The authors of [34] substantiates this claim by comparing the critical temperature of an ultralight boson gas undergoing pair production with the cosmic microwave background temperature.

A quantum mechanical derivation for Eq. (1) could then depart from a second quantized many-body Hamiltonian which is subsequently reduced to an effective Hamiltonian for the order parameter, i.e., the condensate wave function Ψ, [4]. The result would be again Eq. (1) with $\hbar$ as Planck's constant.

We return to this quantum mechanical interpretation in Sec. III when the time integration is formulated as approximation to time evolution operator or in Sec. II C 1 when the quantum virial theorem is used to analyze the long term FDM dynamics.

Smoothed CDM dynamics.—On the other hand, if we accept Eq. (1) as an abstract evolutionary problem and forget momentarily about its interpretation as alternative dark matter model, the dynamics of Ψ can be associated with a *smoothed* version of the Vlasov-Poisson equation (VP)—the phase space description of CDM [22–24].

More precisely, if $f_V(\boldsymbol{x}, \boldsymbol{p})$ denotes the solution to VP and $f_W(\boldsymbol{x}, \boldsymbol{p})$ the Wigner phase space distribution, constructed from Ψ via

$$f_W(\boldsymbol{x}, \boldsymbol{p}) = \int d^3x' \Psi\left(\boldsymbol{x} - \frac{\boldsymbol{x}'}{2}\right)\Psi^*\left(\boldsymbol{x} + \frac{\boldsymbol{x}'}{2}\right) e^{\frac{i}{\hbar}\boldsymbol{p}\cdot\boldsymbol{x}'},$$

then the evolution of the smoothed, or convolved, distributions,

$$\bar{f}_{V/W}(\boldsymbol{x}, \boldsymbol{p}) = \exp\left(-\frac{\boldsymbol{x}^2}{2\sigma_x^2} - \frac{2\sigma_x^2}{\hbar^2}\boldsymbol{p}^2\right) * f_{V/W}, \qquad (5)$$

obeys [23]

$$\partial_t(\bar{f}_W - \bar{f}_V) = \frac{\hbar^2}{24}\partial_{x_i}\partial_{x_j}\nabla_x\bar{V}\partial_{p_i}\partial_{p_j}\nabla_p\bar{f}_W + \mathcal{O}(\hbar^4, \hbar^2\sigma_x^2).$$

Here, $\hbar$ is *not* Planck's constant and $\hbar/m$ acts as a model parameter that sets the maximum phase space resolution.

Then, σ_x is a artificial smoothing scale in comoving position space.

In that sense, Eq. (1) can be understood as an alternative sampling of the CDM distribution compared to the N-body approach: Instead of following the evolution of N test particles sampling f_V, we coarse grain the phase space distribution directly and use Ψ as a dynamical proxy for its evolution. See Sec. II C 2 for an application of this interpretation.

3. Dynamics in the linear regime

The behavior of FDM in the linear growth regime is well-established in the literature; see e.g., [33–35]. We are therefore brief and only focus on aspects relevant for our interpretation of the numerical simulations later on in Sec. IV A.

In short, Madelung's ansatz, [36], of decomposing the wave function into $\Psi(\boldsymbol{x}, t) = \sqrt{\rho(\boldsymbol{x}, t)} \exp\left(i \frac{S(\boldsymbol{x},t)}{\hbar}\right)$, turns Eq. (1) into the Euler-Poisson (EP) equation including an additional (quantum) pressure term,

$$\partial_t \rho + \frac{1}{a} \nabla \cdot (\rho \boldsymbol{v}) = 0, \tag{6a}$$

$$\triangle \Phi = \frac{4\pi G}{a} (\rho - \rho_m), \tag{6b}$$

$$\partial_t \boldsymbol{v} + \frac{1}{a} (\boldsymbol{v} \cdot \nabla) \boldsymbol{v} + H \boldsymbol{v} = -\frac{1}{a} \nabla \Phi + \frac{\hbar^2}{2m^2 a^3} \nabla \left(\frac{\triangle \sqrt{\rho}}{\sqrt{\rho}} \right). \tag{6c}$$

Note that in order to pass from SP to EP we assumed $\psi \neq 0$ and identified the phase function $S(\boldsymbol{x}, t)$ as potential of the peculiar velocity $\boldsymbol{v}$,

$$\boldsymbol{v} \equiv \frac{1}{ma} \nabla S = \frac{\hbar}{ma|\Psi|^2} \mathrm{Im}(\Psi^* \nabla \Psi). \tag{7}$$

Adding this condition to EP makes all solutions to Eqs. (6a)–(6c) irrotational, i.e., $\nabla \times \boldsymbol{v} = 0$, by construction. It is worth pointing out that SP and EP, if considered in isolation, support solutions with nonvanishing circulation. These so-called vortices play an instrumental role for the energy transport in classical, turbulent flows [37] and Bose-Einstein condensates [38,39]. The distinctive property of vortices governed by SP is their quantized circulation. This physical constraint is missing in the classical, hydrodynamical equations and needs to be added by hand to EP in order to establish a formal SP–EP equivalence; see Ref. [40].

Linearizing Eqs. (6a)–(6c) up to first order in $\boldsymbol{v}$ and $\rho(\boldsymbol{x}, t) = \rho_m(1 + \delta(\boldsymbol{x}, t))$ yields a damped oscillator equation for the density contrast δ in the reciprocal domain,

$$0 = \partial_t^2 \hat{\delta} + 2H(t) \partial_t \hat{\delta} - \frac{4\pi G \rho_m}{a^3} \left[1 - \left(\frac{k}{k_J(a)} \right)^4 \right] \hat{\delta} \tag{8}$$

$$\text{with} \quad k_J(a) = \left(\frac{16\pi G \rho_m m^2 a}{\hbar^2} \right)^{\frac{1}{4}}, \tag{9}$$

and $\hat{\delta} = \hat{\delta}(k, t)$. As for CDM, no mode coupling occurs and all perturbations evolve independently under FDM evolution. However, in contrast to CDM, large and small scale modes behave differently. Most notably, Eq. (9) defines a time-dependent critical length scale, $\lambda_J(a) = 2\pi/k_J(a)$,—the Jeans scale—below which the quantum pressure counteracts gravity so that density perturbations do not collapse under their self-gravity.

The linear Jeans scale can also be understood as a consequence of Heisenberg's uncertainty principle, [12], $m\sigma_r \sigma_v \simeq \hbar$. In hydrodynamic terms σ_v may be interpreted as a velocity dispersion and a simple way to estimate it in the linear regime is to follow a particle trapped inside a gravitational well of a matter distribution with density ρ_m,

$$\sigma_v \approx \frac{r}{t_{\mathrm{dyn}}} \approx ax\sqrt{G\rho_m a^{-3}},$$

with t_{dyn} as dynamical time scale estimate. Thus,

$$\sigma_x \simeq \frac{\hbar}{mx\sqrt{G\rho_m a}}.$$

Setting $x = \sigma_x$ yields Eq. (9) up to a numerical constant of $\mathcal{O}(1)$.

The interpretation then is that the source of the quantum pressure is Heisenbergs uncertainty principle which induces an increasing velocity dispersion in the FDM condensate once particles are confined to a space region that is comparable to σ_x.

Although, the Jeans length of Eq. (9) is a purely linear concept, the uncertainty principle is not. One should therefore expect a distinct signature in the matter power spectrum, even deeply in the nonlinear regime. We return to this in Sec. IV A 3.

Once a perturbation mode $\hat{\delta}(k, t)$ leaves the linear regime, Eq. (8) is not applicable anymore. One then expects mode coupling to take place and thus a redistribution of power across all scales that participate in the nonlinear evolution. The implications of this effect will be analyzed in Sec. IV A 4.

B. Fuzzy dark matter in (1 + 1) dimensions

Let us now turn the attention to one-dimensional approximations to $(3 + 1)$-SP and how such models may be deduced from Eq. (1). A convenient starting point for the dimension reduction procedure is to subsume Eqs. (3)–(4) into a single dimensionless, nonlinear Schrödinger

equation (NLSE). This simplifies the discussion and is achieved by (i) absorbing the solution of Poisson's equation by means of a convolution integral and (ii) adopting dimensionless quantities. One arrives at

$$i\hbar\partial_t\Psi = \left[-\frac{1}{2}\triangle + a(t)(G^{\mathrm{ppp}}_{\triangle_3} * |\Psi|^2)\right]\Psi \qquad \boldsymbol{x}\in\Omega, \quad (10)$$

where we defined

$$\boldsymbol{x}' \equiv \left(\frac{m}{\hbar}\right)^{\frac{1}{2}}\left[\frac{3}{2}H_0^2\Omega_m\right]^{\frac{1}{4}}\boldsymbol{x}, \qquad \mathrm{d}t' \equiv \frac{1}{a^2}\left[\frac{3}{2}H_0^2\Omega_m\right]^{\frac{1}{2}}\mathrm{d}t,$$

$$\Psi'(\boldsymbol{x}',t') \equiv \frac{\Psi(\boldsymbol{x}',t')}{\sqrt{\rho_m}}, \qquad V(\boldsymbol{x}',t') \equiv a\frac{m}{\hbar}\left[\frac{3}{2}H_0^2\Omega_m\right]^{-\frac{1}{2}}\Phi,$$

and dropped all primes subsequently. The nonlinear potential is then given by

$$G^{\mathrm{ppp}}_{\triangle_3} * |\Psi|^2 = \int_\Omega \mathrm{d}^3x' G^{\mathrm{ppp}}_{\triangle_3}(\boldsymbol{x}-\boldsymbol{x}')|\Psi(\boldsymbol{x}')|^2,$$

and $G^{\mathrm{ppp}}_{\triangle_3}$ denotes the Green's function of the $d=3$ Poisson equation augmented with periodic boundary conditions in all three dimensions. Equation (10) takes the form of a nonautonomous, i.e., explicitly time-dependent, NLSE with a long range (i.e., nonlocal) interaction kernel.

We stress $G^{\mathrm{ppp}}_{\triangle_3}(\boldsymbol{x},\boldsymbol{x}')$ is *not* the canonical $1/r$-potential as it lacks the required periodicity and only applies under free space boundary conditions, $\lim_{|\boldsymbol{x}|\to\infty}|\boldsymbol{x}|V(\boldsymbol{x}) = -\frac{1}{4\pi}$, see [41]. Instead, we have

$$G^{\mathrm{ppp}}_{\triangle_3}(\boldsymbol{x},\boldsymbol{x}') = \frac{1}{L_1L_2L_3}\sum_{\|\boldsymbol{n}\|>0}\frac{-1}{\boldsymbol{k}^2}e^{i\boldsymbol{k}\cdot(\boldsymbol{x}-\boldsymbol{x}')}, \qquad (11)$$

with $\boldsymbol{n}\in\mathbb{Z}^3$, $\boldsymbol{k}\in\mathbb{R}^3$ and $k_i = \frac{2\pi}{L_i}n_i$.

The Newtonian $1/r$-potential may be recovered as free-space limit in two stages. By first taking $L_{1,2}\to\infty$ [42] recasts Eq. (11) into

$$G^{\mathrm{ppp}}_{\triangle_3}(\boldsymbol{x},\boldsymbol{x}') \xrightarrow{L_{1,2}\to\infty} G^{\mathrm{ffp}}_{\triangle_3}(\boldsymbol{x},\boldsymbol{x}') = \frac{1}{2\pi L_3}\log|\boldsymbol{x}_\perp - \boldsymbol{x}'_\perp|$$

$$-\frac{1}{\pi L_3}\sum_{m=1}^\infty \cos\left(k_m(x_3 - x'_3)\right)K_0(k_m|\boldsymbol{x}_\perp - \boldsymbol{x}'_\perp|), \qquad (12)$$

with $K_0(x)$ denoting the 0th-modified Bessel function of the second kind and $\boldsymbol{x}_\perp = (x_1, x_2)^\intercal$. We return to this mixed boundary condition Green's function in Sec. II B 2 b. Finally, take $L_3\to\infty$ so that the Riemann sum in Eq. (12) approaches an analytically solvable integral [43],

$$G^{\mathrm{ffp}}_{\triangle_3}(\boldsymbol{x},\boldsymbol{x}') \xrightarrow{L_3\to\infty} G^{\mathrm{fff}}_{\triangle_3}(\boldsymbol{x},\boldsymbol{x}') = -\frac{1}{4\pi|\boldsymbol{x}-\boldsymbol{x}'|},$$

yielding the expected result.

The naive way of carrying out the dimension reduction of Eq. (10) is to simply drop all partial derivatives in x_1, x_2-direction. This appears to be the common approach in low-dimensional studies on FDM [22,24,34,44–46] and turns out to be true assuming we demand a *uniform* matter distribution along the neglected dimensions. The approach is equally applicable for $d=1,2$ and leads to the $(d+1)$-SP equation.

Maintaining Poissons equation as field equation has implications on how gravity acts in lower dimensions since the periodic Greens function in Eq. (11) depends on the dimensionality of the Laplace operator. We stress even if the aforementioned violation of the periodic boundary conditions would not exist for the Newtonian potential, it would still be impossible to simply enforce a $1/r$-interaction kernel in one dimension. Its singularity at the origin remains too strong and consequently yields an ill-defined convolution kernel. Hence, we ask whether a reduction exists that approximately preserves the three-dimensional interaction with only one spatial degree of freedom. This is realized by *strongly confining* matter orthogonal to the dimension in which the evolution is observed.

1. General reduction procedure

We adapt the discussion under free-space conditions outlined in [47] to the periodic situation at hand. To this end, the NLSE in Eq. (10) is augmented by an artificial, external potential $\mathcal{V}_{\mathrm{ext}}(\boldsymbol{x}_\perp; \epsilon) = \frac{1}{\epsilon^2}V_{\mathrm{ext}}(\frac{\boldsymbol{x}_\perp}{\epsilon})$ in the orthogonal $\boldsymbol{x}_\perp$-plane that is controlled by a confinement parameter ϵ. The extended Hamiltonian $H = H_{x_3} + H^\epsilon_\perp$ is then decomposed into

$$H_{x_3} = -\frac{1}{2}\partial^2_{x_3} + a(t)(G^{-\mathrm{p}}_{\triangle_3} * |\Psi|^2),$$

$$H^\epsilon_\perp = \frac{1}{\epsilon^2}\left[-\frac{1}{2}\triangle_{\bar\perp} + V_{\mathrm{ext}}(\boldsymbol{x}_{\bar\perp})\right] = \frac{1}{\epsilon^2}H_{\bar\perp},$$

with $\boldsymbol{x}_{\bar\perp} = \boldsymbol{x}_\perp/\epsilon$. Notice how we keep the boundary conditions of the interaction kernel $G^{-\mathrm{p}}_{\triangle_3}$ deliberately unspecified in the $\boldsymbol{x}_\perp$-plane. These will be set in accordance with the external potential, i.e., if $V_{\mathrm{ext}}(\boldsymbol{x}_\perp)$ is periodic on $\Omega_1\times\Omega_2$, the long range interaction is $G^{\mathrm{ppp}}_{\triangle_3}$, as in Eq. (11). If, however, the external potential assumes free-space conditions, the reduction departs from the mixed condition Green's function $G^{\mathrm{ffp}}_{\triangle_3}$ in Eq. (12).

Next, find the eigensystem $\{\chi^\epsilon_k, \lambda^\epsilon_k\}$ to the linear eigenvalue problem $H^\epsilon_\perp\chi^\epsilon_k(\boldsymbol{x}_\perp) = \lambda^\epsilon_k\chi^\epsilon_k(\boldsymbol{x}_\perp)$ and enforce a factorization of the full fledged wave function $\Psi(\boldsymbol{x},t)$ according to $\Psi(\boldsymbol{x},t) = \psi(x_3,t)\chi^\epsilon_k(\boldsymbol{x}_\perp)e^{-i\lambda^\epsilon_k t}$. Insert this

ansatz into the NLSE with the extended Hamiltonian, multiply by $(\chi_k^\epsilon)^*$ and integrate over the $\boldsymbol{x}_\perp$-plane. The result is a one-dimensional NLSE for $\psi(x_3, t)$,

$$i\hbar\partial_t\psi = \left[-\frac{1}{2}\partial_{x_3}^2 + a(t)(U^{\mathrm{p}} * |\psi|^2)\right]\psi \quad x_3 \in \Omega_3, \quad (13)$$

alongside a one-dimensional, long range interaction, U^{p},

$$U^{\mathrm{p}}(x_3, x_3') = \frac{1}{\|\chi_k^\epsilon\|_2^2} \int_{\Omega_1 \times \Omega_2} \mathrm{d}^2 x_\perp'$$
$$\times \int_{\Omega_1 \times \Omega_2} \mathrm{d}^2 x_\perp |\chi_k^\epsilon(\boldsymbol{x}_\perp)|^2 |\chi_k^\epsilon(\boldsymbol{x}_\perp')|^2$$
$$\times G_{\triangle_3}^{-\mathrm{p}}(\boldsymbol{x}_\perp, x_3, \boldsymbol{x}_\perp', x_3'). \quad (14)$$

Since the spectrum of Eq. (11) is spherical symmetric around $\boldsymbol{k} = 0$ it is clear that, irrespective of the confining potential in the transversal plane, the one-dimensional interaction kernel remains even and depends only on the relative distance: $U^{\mathrm{p}}(x_3, x_3') = U^{\mathrm{p}}(|x_3 - x_3'|)$.

2. Uniform vs confined transversal density

Let us restrict the discussion to two distinct external potentials that either induce a complete delocalization of matter in the orthogonal plane or constrain all matter around the x_3-direction. In what follows, both of these models will be coined $(1+1)$-FDM collectively. If a distinction has to be made, a more precise denotation will be used.

Uniform matter.—Set $V_{\mathrm{ext}} = 0$. The corresponding eigenstates are plane waves, and matter is therefore assumed to be organized in homogeneous matter sheets parallel to the $\boldsymbol{x}_\perp$-plane. Moreover, the external potential is trivially L_3-periodic so that $G_{\triangle_3}^{-\mathrm{p}} = G_{\triangle_3}^{\mathrm{ppp}}$. Equation (14) then evaluates to [43]

$$G_{\triangle_1}^{\mathrm{p}}(x_3, x_3') = \frac{1}{2}|x_3 - x_3'| - \frac{1}{2}\left[\frac{(x_3 - x_3')^2}{L_3} + \frac{L_3}{6}\right], \quad (15)$$

i.e., the Green's function of the $d = 1$ Poisson equation under periodic boundary conditions.

Equation (13) together with the interaction of Eq. (15) is denoted $(1+1)$-SP.

Confined matter.—We enforce an integrable harmonic confining potential $V_{\mathrm{ext}}(\boldsymbol{x}_\perp) = \frac{1}{2}\boldsymbol{x}_\perp^2$ and consider only the ground state $\chi_0(\boldsymbol{x}_\perp) \propto \exp(-\boldsymbol{x}_\perp^2/2)$ for the dynamics in the orthogonal plane. Our choice is motivated by cigar-shaped confinements often used for trapping Bose-Einstein condensates; see e.g., [3,48–52]. Neither the external potential nor its ground state are periodic. Hence, we set $G_{\triangle_3}^{-\mathrm{p}} = G_{\triangle_3}^{\mathrm{ffp}}$ in Eq. (14) and find
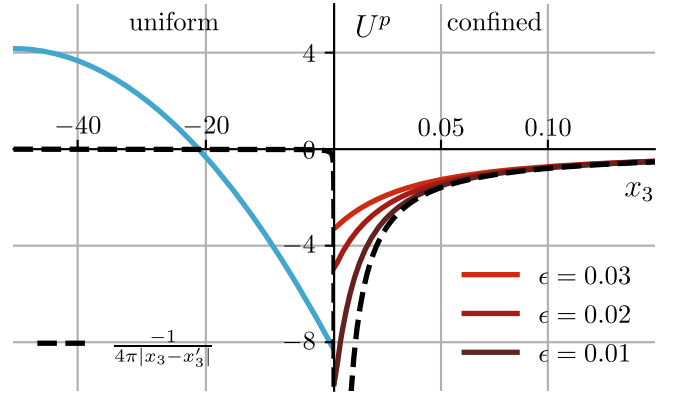

FIG. 1. Comparison of the one-dimensional, long range interactions of Sec. II B 2 a and Sec. II B 2 b induced by a source particle located at $x_3 = 0$ in a periodic box of $L_3 = 100$. The negative x-space illustrates the situation for a uniform matter distribution in the transversal plane with $G_{\triangle_1}^{\mathrm{p}}$, Eq. (15), as gravitational potential (blue line). The positive x-space depicts the gravitational potential $U_{\mathrm{conf}}^{\mathrm{p}}$, Eq. (16), obtained under harmonic confinement for various confinement strengths ϵ (red lines). While both $G_{\triangle_1}^{\mathrm{p}}$ and $U_{\mathrm{conf}}^{\mathrm{p}}$ are finite at the origin only $U_{\mathrm{conf}}^{\mathrm{p}}$ approaches the Newtonian gravitational potential (black, dashed line) in the far field. Note the different limits of the negative and positive x_3-axis: The negative half space covers the interval $[-L_3/2, 0]$, the positive half space is truncated at $x_3 = 0.15$ to make the asymptotic behavior of $U_{\mathrm{conf}}^{\mathrm{p}}$ better observable.

$$U_{\mathrm{conf}}^{\mathrm{p}}(x_3, x_3') = \frac{-1}{4\pi L_3}\sum_m U\left(1, 1, \frac{1}{2}k_m^2\epsilon^2\right)e^{ik_m(x_3 - x_3')}, \quad (16)$$

with $m \in \mathbb{Z}\backslash 0$ and $U(a, b, x)$ denoting the confluent hypergeometric function of the second kind [53].

Consider Fig. 1 for a graphical comparison of the long range interaction induced by a test particle at $x_3' = 0$ with and without confinement. All potentials are shown for a periodic box of $L_3 = 100$. Apart from the required finiteness of both kernels at the origin, the behavior of $U_{\mathrm{conf}}^{\mathrm{p}}$ and $G_{\triangle_1}^{\mathrm{p}}$ is quite disparate in the far-field region. A key difference lies in the effective interaction range R which may be defined as

$$\partial_r U^p(R) \equiv \delta \max|\partial_r U^p| \quad \text{with} \quad 0 < \delta \ll 1. \quad (17)$$

While the gravitational potential under confinement is rather localized with $R \sim \epsilon$ and quickly approaches the desired Newtonian potential (black, dashed line) at large distances $|x_3 - x_3'|$, the effective interaction range for $G_{\triangle_1}^{\mathrm{p}}$ evaluates to $R = \frac{1}{2}(1 - \delta)L_3$ and is therefore comparable to the box size. As discussed in Sec. IV B 4, this has implications on which asymptotic states are accessible in the $(1+1)$-SP case.

3. Symmetries and conserved quantities

Naturally, one is interested in conserved quantities of Eq. (13) for even kernels but irrespective of its exact form. By analyzing the action,

$$S = \int dt \int_{\Omega_3} dx_3 (i\psi^* \partial_t \psi - \mathcal{H}[\psi, \psi^*, \partial_{x_3}\psi, \partial_{x_3}\psi^*, t]),$$

(18)

with the Hamiltonian density,

$$\mathcal{H} = \frac{1}{2}(|\partial_{x_3}\psi|^2 + a(t)(U^p * |\psi|^2)|\psi|^2)$$

generating Eq. (13) upon variation, it is straightforward to show that such a system obeys mass and momentum conservation. Moreover, Eq. (18) is invariant under galilean boosts of the form,

$$\psi(x, t) \rightarrow e^{i(vx_3 - \frac{1}{2}v^2 t)}\psi(x_3 - vt, t).$$

(19)

If we consider a *static* space-time, i.e., $a(t) = \text{const}$, Eq. (18) is also time translation invariant and the total energy,

$$E[\psi] = \int_{\Omega_3} dx_3 \mathcal{H}[\psi, \psi^*, \partial_{x_3}\psi, \partial_{x_3}\psi^*, t] = \langle T \rangle + \frac{a}{2}\langle V \rangle,$$

(20)

is conserved as well. This is of course *not* true once space-time is allowed to expand.

A symmetry unique to $(1+1)$-SP is the following scaling transformation: If $\psi(x_3, t)$ solves Eq. (13) with $U^p = G^p_{\triangle_1}$ then so does

$$\tilde{\psi}(x_3, t) = \lambda^2 \psi(\lambda x_3, \lambda^2 t), \quad \lambda \in \mathbb{R}^+.$$

(21)

Equivalent scaling symmetries exist for $d = 2, 3$ spatial dimensions [28].

4. Properties of the $(1+1)$-FDM ground state

We already alluded in our introductory remarks to the importance of stationary states of $(3+1)$-SP, especially the role of its stable ground state that acts as dynamical attractor and realizes a flat-density core inside relaxed dark matter structures. Let us extend this discussion to the previously derived one-dimensional FDM models by analyzing properties of the ground state to Eq. (13) that influence the asymptotic $(1+1)$-FDM dynamics.

For practical purposes, ground states of mass $N[\psi] = \int dx_3 |\psi|^2 = M$ may be prepared by choosing an interaction kernel and minimizing the grand canonical energy $E_{\text{grand}}[\psi] = E[\psi] + \mu(\tau)N[\psi]$ by means of a gradient descent with $\mu(\tau)$ as chemical potential at descent
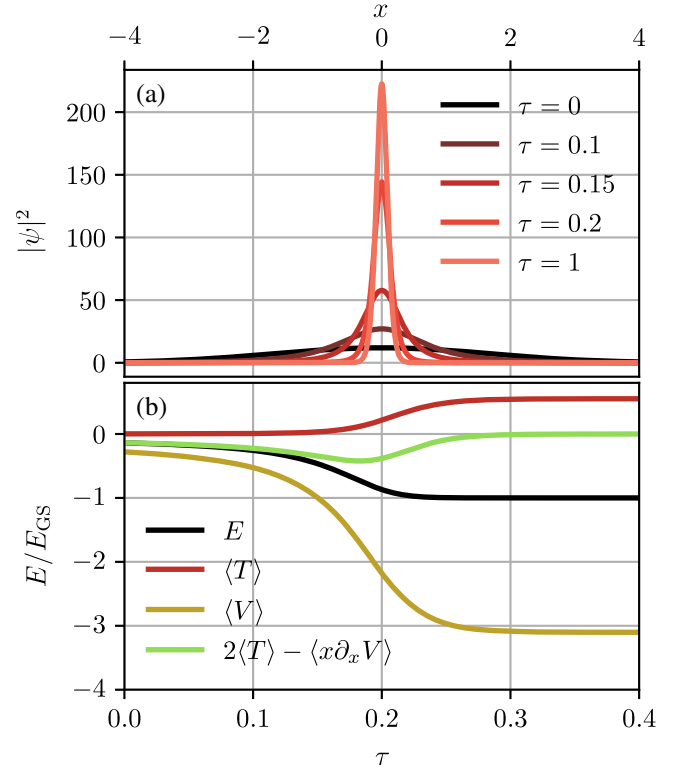

FIG. 2. Exemplary gradient descent for $U^p = U^p_{\text{conf}}$, i.e., under confinement, with ground state mass $M = 50$, $a = 1$ and $\epsilon = 10^{-2}$. (a) Densities at various stages of the minimization procedure. (b) Evolution of kinetic (red), potential (yellow) and total energy (black) normalized to the ground state energy E_{GS}. Also shown in green is the free-space, quantum virial theorem, discussed in Sec. II C 1.

parameter τ. The reader is referred to [54,55] for numerical details and [56] for a rigorous analysis on the existence and uniqueness of a minimizer to Eq. (20) for $(1+1)$-SP under free-space conditions. We note in passing that the chosen numerical implementation of the gradient descent makes the energy minimization approach equivalent to the well-known imaginary time propagation method [52,57].

An exemplary gradient descent under transversal, harmonic confinement is depicted in Fig. 2. As time progresses the initial Gaussian distribution focuses more and more in position space until the descent converges to a spatially localized structure at $\tau = 1$.

Irrespective whether $U^p = U^p_{\text{conf}}$ or $U^p = G^p_{\triangle_1}$, the $(1+1)$-FDM ground state shows the following properties:

Solitary wave.—It is easy to see that the equation governing the gradient descent, namely $\partial_\tau \psi = -\frac{1}{2}\frac{\delta}{\delta\psi}E_{\text{grand}}$, reduces to a stationary form of Eq. (13),

$$\mu(\tau^*)\psi_{\text{GS}} = \left[-\frac{1}{2}\partial_{x_3}^2 + a(U^p * |\psi_{\text{GS}}|^2)\right]\psi_{\text{GS}}, \quad (22)$$
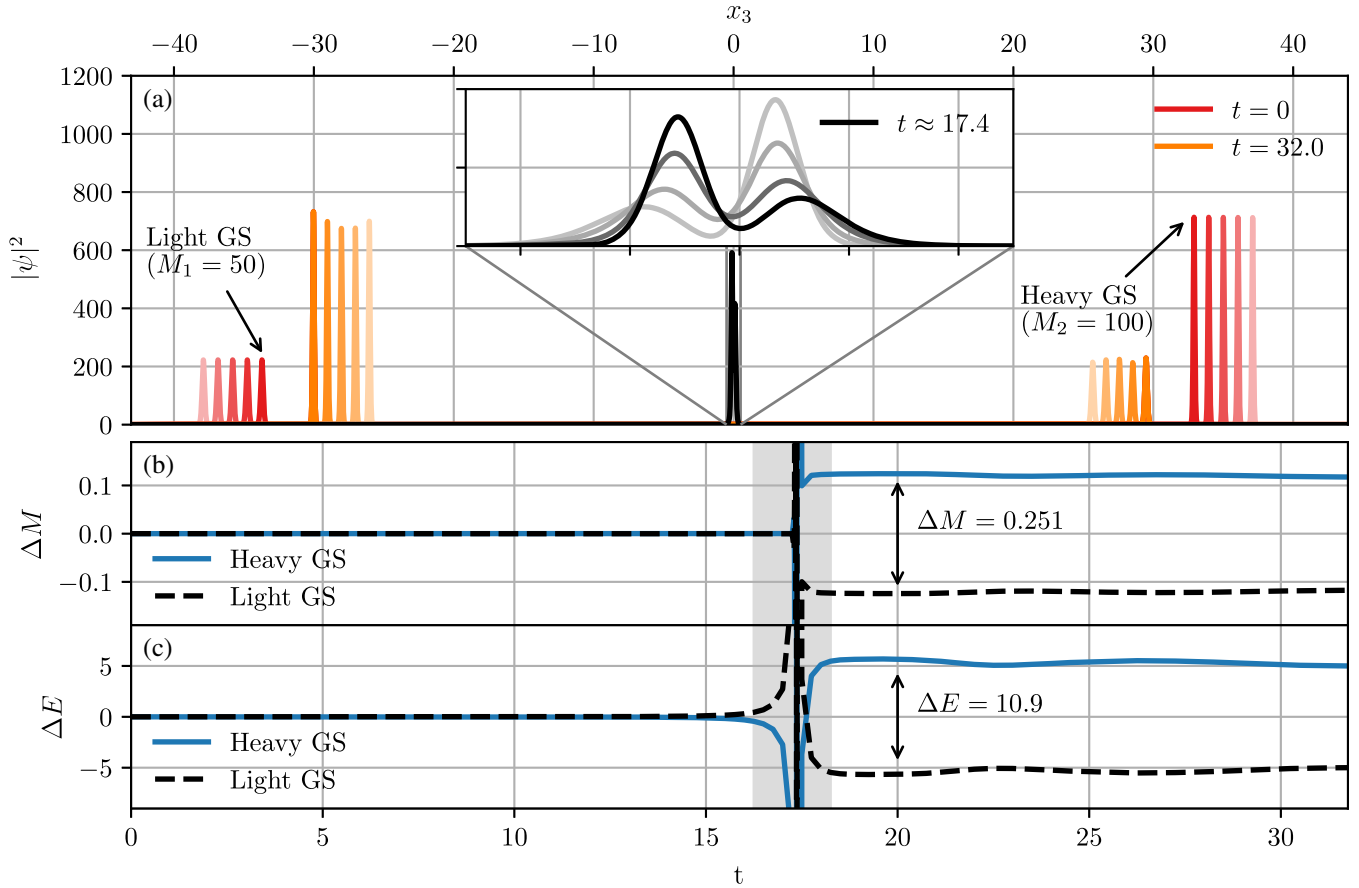
once the energetic minimum at $\tau = \tau^*$ is reached.

FIG. 3. Inelastic interaction of an asymmetric high-mass, low-mass ground state configuration under strong, transversal confinement ($\epsilon = 10^{-2}$) and $a = 1$. The evolution starts from Eq. (23). (a) Density evolution. Initially, both densities travel as solitary waves (red), pass through each other (black, inset) and continue to propagate in a quasisolitary movement after the interaction (orange). By this we mean a state for which neither linear dispersive nor nonlinear focusing effects induce a permanent deformation of the density. Instead, one observes an oscillation around a solitary wave. Similar oscillatory behavior was found for $(3+1)$-SP, [27], once the ground state density is perturbed. (b) Time evolution of the mass deviation of both ground states relative to their initial masses cf. Eq. (24). Postinteraction, it is the high-mass ground state gaining additional matter at the expense of the lighter ground state. (c) Time evolution of the total energy deviation of both ground states relative to their respective initial total energies. As for the mass, the interaction induces an energy transfer from the low to high mass ground state. Notice, how the quasisolitary behavior of the postinteraction densities is also seen in an oscillation of the energy deviation. Since the association of mass and energy contained in the positive and negative box half to a particular solitary wave is ambiguous during the interaction, we deem data in the gray shaded interval of (b) and (c) as not reliable.

Therefore, the ground state may be written in its canonical, linear quantum mechanics form, $\psi_{GS}(x_3, t) = \psi_{GS}(x_3)e^{-i\mu(\tau^*)t}$, and we conclude ψ_{GS} is a *solitary wave*, i.e., a localized solution to a nonlinear equation with time independent envelope $|\psi|^2$. Obviously, its persistent form is also preserved for uniformly travelling configurations obtained via Eq. (19).

Two remarks are in order: firstly, the above discussion derives ψ_{GS} by minimizing the total energy functional. An alternative approach, e.g., [27], is to interpret the nonlinear eigenvalue problem of Eq. (22) as boundary value problem and solve it via a shooting method. Secondly, recall the scaling symmetry of Eq. (21) unique to $(d+1)$-SP. Applying it to a single ground state gives access to an entire family of ground states parametrized by their total

mass M. Thus, for $(1+1)$-SP, it is sufficient to conduct the energy minimization only once for an arbitrary reference mass M_{ref}. All other energy minimizers then follow from rescaling with Eq. (21). Lacking an equivalent symmetry, this is of course not true for the confinement model.

Inelastic collisions.—So far, we demonstrated the solitary character of the $(1+1)$-FDM ground state. Naturally, we are interested whether ψ_{GS} can also be identified as a solitonic solution.

Strictly speaking, the concept of a soliton calls for a rigorous mathematical definition. To keep technical details to a minimum, we instead follow [58] and characterize a soliton as a solitary wave that is invariant under interactions with other solitons. Put differently, despite the nonlinear

evolution, solitons obey a superposition principle and neither mass nor energy should be exchanged during the interaction.

Figure 3 investigates the behavior of an asymmetric configuration of two confined ground states with initial masses $M_1 = 50$ and $M_2 = 100$ and $\epsilon = 10^{-2}$, boosted onto a collision course with

$$\psi_0(x_3) = \psi_{GS,1}(x_3 + x_0)e^{ivx_3} + \psi_{GS,2}(x_3 - x_0)e^{-ivx_3}. \tag{23}$$

Figure 3(a) depicts the matter density in a precollision time window, an instance during the ground state interaction ($t \approx 17.4$) as well as a postcollision time window around $t = 32$. It is evident that the superposition principle is not satisfied. After the interaction took place both ground states propagate in a quasisolitary fashion in which linear dispersive and nonlinear focusing effects are not exactly balanced anymore. Instead one finds a periodic expansion and recontraction of the matter distribution once the dispersion or nonlocal, nonlinearity dominates. Similar oscillatory behavior was found for the $(3 + 1)$-SP ground state, [27], once the density is perturbed. Nevertheless, on average the postinteraction configuration is still comprised of two solitary, or stationary, states.

To investigate whether these postinteraction, solitary waves are different from their initial composition, we analyze the deviation in mass [Fig. 3(b)] and total energy [Fig. 3(c)] from their initial values. For instance, the mass difference for the M_1-ground is inferred as

$$\Delta M(t) = \int_{-\frac{L_3}{2}\Theta(t_{\mathrm{coll}}-t)}^{\frac{L_3}{2}\Theta(t-t_{\mathrm{coll}})} dx_3 |\psi(x_3, t)|^2 - M_1, \tag{24}$$

with t_{coll} as collision time naively inferred from the uniform velocity v at $t = 0$.

One finds a symmetric mass and energy gap after the interaction: Both mass and energy were transferred from the low to high mass solitary wave. Clearly, such a matter and energy transfer should not exist if the confined ground state were a true soliton. We note although the reported energy and mass differences are small they are robust under variation of Δt; see Sec. III B for more information. Qualitatively similar results were found for $(1 + 1)$-SP. Therefore, $(1 + 1)$-FDM ground states—at least the ones considered here—are *not* solitons in the strict sense of the word, but interact inelastically by exchanging mass and energy during encounters, typically reshuffling them from the low-mass to the high-mass solitary wave.

Of particular interest is the case of multiple successive interactions which, thanks to the periodicity of the box, is easily observed by increasing the integration time. The reader is referred to Sec. IV B 2 for more details.
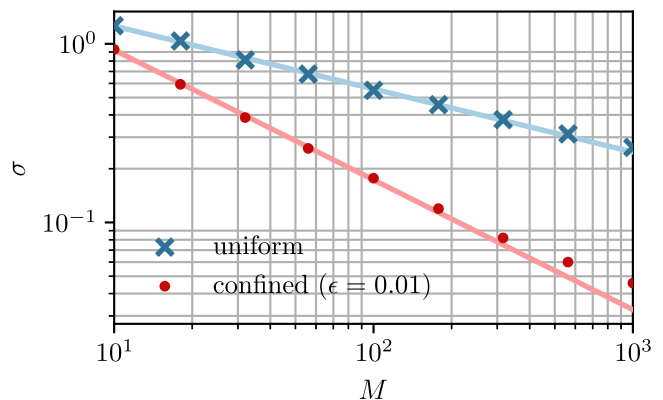

FIG. 4. Spatial extent of the one-dimensional FDM ground states as a function of mass M at $a = 1$. Each data point corresponds to a solitary wave prepared by the gradient descent shown in Fig. 2. The spatial extent of the matter distribution is extracted according to Eq. (25). For $U^{\mathrm{p}} = G^{\mathrm{p}}_{\triangle_1}$ (blue) we find $\sigma(M) = 2.8 \cdot M^{-0.34}$ and consequently good agreement with dimensional analysis. Under strong harmonic confinement, i.e., $U^{\mathrm{p}} = U^{\mathrm{p}}_{\mathrm{conf}}$ and $\epsilon = 10^{-2}$ (red) one deduces $\sigma(M) = 4.9 \cdot M^{-0.72}$ over 2 orders of magnitude in M.

Mass-size relation.—As we will see, understanding the discrepancies between the attained asymptotic states of $(1 + 1)$-SP and the confinement model, Sec. IV B 4, hinges on the ratio $R(L_3)/\sigma(M)$, i.e., the interaction range R given a periodic box of size L_3 compared to the spatial extent σ of a mass M ground state.

Deriving $\sigma(M)$ is particularly simple in case of the unconfined FDM model as Madelung's ansatz relates $(1 + 1)$-SP to a one-dimensional version of the hydrodynamic description of Eqs. (7)–(6c). In the ground state's rest frame these reduce to the condition of hydrostatic equilibrium. Dimensional analysis then yields $\sigma \propto M^{-\frac{1}{3}}$.

The situation is more involved under harmonic confinement due to the missing partial differential equation for the gravitational potential. Thus, the spatial extent is deduced numerically by defining

$$0.99M \equiv \int_{-\sigma}^{\sigma} dx_3 |\psi_{GS}|^2, \tag{25}$$

and extracting σ for various, spatially centered ground states of mass M. Figure 4 depicts the result for a static space-time with $a = 1$ for both $(1 + 1)$-FDM models. While $(1 + 1)$-SP shows satisfactory agreement with the dimensional analysis, $\sigma(M) = 2.8 \cdot M^{-0.34}$, a strongly confined matter density at $\epsilon = 10^{-2}$ results in a narrower ground state distribution at equal mass M. In this case $\sigma(M) = 4.9 \cdot M^{-0.72}$.

C. Relaxation mechanisms and equilibrium properties

It is *a priori* not clear what dynamical mechanisms drive $(1 + 1)$-FDM into its asymptotic equilibrium configuration let alone whether both reduction models obey the same

relaxation processes—recall the discrepancies in the interactions of $(1 + 1)$-SP and the confinement scenario.

Given the approximative CDM interpretation of FDM in Sec. II A 2 b, classical, noncollisional relaxation mechanism may be a viable option, in particular a combination of phase mixing and violent relaxation; see [59,60]. These processes induce a filamentation of the phase space dynamics alongside a redistribution of energy inside the self-gravitating structure due to its fluctuating gravitational potential.

On the other hand, $(3 + 1)$-FDM-typical mechanisms like gravitational cooling, [30], may be recovered even in one dimension, allowing collapsing matter structures to relax into an equilibrated state by radiating away excess energy in form of small scale matter waves.

Which relaxation channels are realized is discussed in Sec. IV B 2. Here, we ask what properties the equilibrated system configuration should have and how they may be measured such that the progress on the overall system evolution can be quantified.

1. Virial equilibrium

Application of Ehrenfest's Theorem for the virial operator $\hat{G} = \hat{p}\,\hat{x}$ gives rise to a quantum analogue of the scalar virial theorem. For bounded dynamics, i.e., $\langle \hat{G} \rangle(t) < \infty$, and *periodic* boundary conditions it reads

$$0 = 2(\langle T \rangle)_\infty - (a \langle x_3 \partial_{x_3} V \rangle)_\infty$$
$$+ \frac{L}{2}((\psi^*(0,t)\partial_{x_3}^2\psi(0,t) - |\partial_{x_3}\psi(0,t)|^2)_\infty \quad (26)$$

with $(A)_\infty = \lim_{t\to\infty} \frac{1}{t}\int_0^t dt' A(t')$. Relaxation into virial equilibrium, i.e., the regime where Eq. (26) is (approximately) satisfied, is then to be understood as a consequence of the evolution under Schrödingers equation. That said, any finite quantum system would virialize in the limit $t \to \infty$.

A couple of remarks are in order. Firstly, note Eq. (26) only holds in the limit $t \to \infty$. A notable exception are stationary states, like the $(1 + 1)$-FDM ground states of Sec. II B 4, which obey Eq. (26) without time averaging cf. [61]. If in addition fluctuations are present, we may assess virialization of the total system by assuming Eq. (26) were approximately achieved after a finite thermalization time.

Secondly, we draw special attention to the boundary term,

$$B(t) = \psi^*(0,t)\partial_{x_3}^2\psi(0,t) - |\partial_{x_3}\psi(0,t)|^2, \quad (27)$$

in Eq. (26). It emerges from the necessity to extend the domain of the Hamiltonian onto states like $x\psi$ which are not periodic but appear once Ehrenfest's theorem is applied to $\hat{G}$; see [62]. Obviously, the boundary term is negligible,

if ψ decays rapidly towards the box boundaries, like in Fig. 2, or when artificial absorbing potentials are used to limit the physically relevant domain size; see e.g., [17,29].

2. Maximum entropy

From a statistical physics viewpoint, one generally expects the system to maximize its entropy. In fact, the idea of entropy maximization is close to the original approach of [59], showing that mixing processes under Vlasov-Poisson imply a quasistationary phase-space distribution that maximizes the system's entropy on a macroscopic, i.e., coarse-grained level.

To adopt this idea for FDM, we use Husimi's distribution, i.e., $\bar{f}_W$ in Eq. (5) and define a FDM entropy functional resembling Boltzmann's entropy [63],

$$S[\bar{f}_W] = -\frac{1}{2\pi}\int dx_3 dk_3 \bar{f}_W \log \bar{f}_W. \quad (28)$$

Thus, an equilibrated, thermalized system state is reached, once $\Delta S = S(t) - S(0)$ saturates. We note this approach was also proposed by [24].

III. NUMERICAL METHOD

We briefly explain a simple, yet accurate spatial discretization of Eq. (13) and sketch an approximation to its time evolution operator. The main properties of the presented method are summarized. For more information, especially on the method's behavior under expanding space-time conditions, the reader is referred to the Appendix. Additional information on general NLSE numerics can be found in [64]. A recent survey of existing numerical techniques on our subject is given by [65].

A. Spatial discretization

Since Eq. (13) is defined on a periodic domain and involves only second derivatives in space, expansion of ψ in a truncated momentum eigenstate basis is a natural way to discretize Eq. (13) in momentum space and diagonalize the kinetic part of the Hamiltonian. Discreteness in real space is then achieved by evaluating the momentum state expansion of ψ on sites $\{x_j\}_{j=0\ldots N-1}$ with uniform spacing $\Delta x = L/N$. This translates Eq. (13) into the finite dimensional, ordinary differential equation,

$$i\partial_t \boldsymbol{\psi}(t) = \left[\underbrace{\mathcal{F}^\dagger \frac{\boldsymbol{k_3 k_3^\intercal}}{2}\mathcal{F}}_{\hat{H}_K} + \underbrace{a(t)\boldsymbol{V}(|\boldsymbol{\psi}(t)|^2)}_{\hat{H}_V(t,|\boldsymbol{\psi}|^2)}\right]\boldsymbol{\psi}(t), \quad (29)$$

with $\boldsymbol{\psi}_j = \psi(x_j, t)$, $(\boldsymbol{k_3})_n = \frac{2\pi}{L_3}n$ and $\mathcal{F}$ denoting the change of basis matrix from the real space to the momentum basis. In practice the action of $\mathcal{F}$ and its inverse $\mathcal{F}^\dagger$ on $\boldsymbol{\psi}$ are implemented as discrete fast Fourier transform.

The nonlinear, nonlocal potential is absorbed into the diagonal matrix $\boldsymbol{V}(|\boldsymbol{\psi}|^2)$ and follows directly from the convolution theorem,

$$\text{Diag}[\boldsymbol{V}(|\boldsymbol{\psi}(t)|^2)] = \mathcal{F}^\dagger \widehat{\boldsymbol{U}^\pi} \mathcal{F} |\boldsymbol{\psi}(t)|^2,$$

with the, in momentum space diagonal, kernel coefficient matrix $\widehat{\boldsymbol{U}^\pi}$,

$$\text{Diag}[\widehat{\boldsymbol{U}^\pi}] = \begin{cases} 0 & n = 0 \\ -\frac{1}{(k_3)_n^2} & n \neq 0 \, (1+1)\text{SP} \\ -\frac{1}{4\pi} U(1, 1, \frac{1}{2}(k_3)_n^2 \epsilon^2) & n \neq 0 \, \text{confined}. \end{cases}$$

B. Time evolution operator

Starting from Eq. (29) it remains to find an approximation to the time evolution operator $\boldsymbol{\psi}(t + t_0) = \hat{U}_{K+V}(t_0, t_0 + \Delta t)\boldsymbol{\psi}(t_0)$. For this, the idea of operator splitting is employed—a common choice for integrating NLSEs. Thus, we first find (approximate) evolution operators for the kinetic, $\hat{H}_K$, and potential Hamiltonian, $\hat{H}_V$, individually and combine them into an approximation for $\hat{U}_{K+V}$ afterwards.

The solution to the kinetic problem is trivial and reads

$$\hat{U}_K(\Delta t) \equiv \hat{U}_K(t_0, t_0 + \Delta t) = \mathcal{F}^\dagger \exp\left[-i\frac{\boldsymbol{k_3}\boldsymbol{k_3}^\mathsf{T}}{2}\Delta t\right]\mathcal{F}.$$

For the potential subproblem we recall $\hat{H}_V$ is diagonal in real space, implying $[\hat{H}_V(t), \hat{H}_V(t')] = 0$. Thus, its time evolution operator can be written as $\hat{U}_V(\Delta t) = \exp[-i\int_{t_0}^{t_0+\Delta t} dt \hat{H}_V(t, |\psi(t)|^2)]$, and it remains to approximate the time integral over $\hat{H}_V$.

Fortunately, it is easily verified that evolution under the nonlinear Hamiltonian $\hat{H}_V$ satisfies $\frac{d}{dt}|\psi|^2 = 0$. It is therefore sufficient to substitute $\hat{H}_V(t, |\psi(t)|^2) \rightarrow \hat{H}_V(t, |\psi(t_0)|^2)$ which (i) reduces the task of approximating the time integral over $\hat{H}_V$ to approximating the integral over the scale factor $a(t)$ and (ii) allows for an explicit treatment of the nonlinearity, i.e., without the need to solve a nonlinear system of equations.

Application of the midpoint rule yields the following unitary approximation to $\hat{U}_V(\Delta t)$:

$$\hat{U}_V(\Delta t) = \hat{\mathcal{U}}_V(\Delta t, t_0) + \mathcal{O}(\Delta t^3)$$
$$= \exp\left[-ia\left(t_0 + \frac{\Delta t}{2}\right)\boldsymbol{V}(|\boldsymbol{\psi}(t_0)|^2)\Delta t\right] + \mathcal{O}(\Delta t^3).$$

Finally, after composing both evolution operators in a second order Strang scheme, we arrive at the approximation to $\hat{U}_{K+V}$,

$$\hat{U}_{K+V} = \hat{U}_K\left(\frac{\Delta t}{2}\right) \circ \hat{\mathcal{U}}_V(\Delta t, t_0) \circ \hat{U}_K\left(\frac{\Delta t}{2}\right) + \mathcal{O}(\Delta t^3).$$

C. Summary of properties

The presented method is a simple extension to the kick-drift-kick scheme of [17]. In fact, for static space-times both methods are equivalent. Aside from its implementational simplicity and resemblance of the symplectic leap-frog method, it is unitary by design, explicit, second-order accurate in time, spectrally accurate in space (assuming ψ is smooth) and provides a convenient unified approach for both dimension-reduction models. The computational complexity per integration step is $\mathcal{O}(N \log N)$ due to the fast Fourier transformations, requiring $\mathcal{O}(N)$ memory.

Furthermore, for time-independent, nonlinear coupling constants, the approximate evolution operator is time-symmetric, shows unconditionally stable numerical behavior and conserves energy, Eq. (20), approximately with a bounded error [66].

For nonstatic background cosmologies, time-symmetry and energy conservation are broken by the continuous problem. Concerning stability, our tests indicate an exponentially growing error at high redshifts. We expect this result to be to intrinsic to constant time step integration methods under space-time expansion. Further information on the convergence properties of our numerical method are given in the Appendix.

IV. RESULTS OF NUMERICAL SIMULATIONS

A. Structure growth under (1+1)-SP

We investigate the mean cosmic structure growth in an ensemble of FDM-only universes obeying $(1+1)$-SP. The purpose of this study is to explain characteristic properties of the nonlinear FDM matter power spectrum $P(k) = \langle|\hat{\delta}_k|^2\rangle$.

1. Simulation setup

To this end, we follow the evolution of $\mathcal{N} = 100$ realizations of a Gaussian random field $\delta(x, a_0)$ in a flat, radiation free FLRW background cosmology with $\Omega_m = \Omega_{\text{DM}} + \Omega_{\text{baryon}} = 0.3$, $H_0 = 68$ km s^{-1} Mpc^{-1} and power spectrum,

$$P(k, a_0) = D_0^2(a_0)T_{\text{dim}}^2(k)T_{\text{FDM}}^2(k)P_{\text{CDM}}(k), \quad (30)$$

with $k = |k_3|$. Here, $D_0^2(a_0)$ denotes the linear growth factor; see [67], normalized to unity at $z = 0$, $P_{\text{CDM}}(k)$ the linear CDM power spectrum produced by CAMB, see [68], at redshift $z = 0$, $T_{\text{FDM}}^2(k)$ the CDM to FDM transfer function of [12] and $T_{\text{dim}}^2(k) = \frac{k^2}{2\pi}$ a transfer function reducing the spectrum's dimensionality to 1 spatial degree of freedom. The latter follows from demanding a dimension independent real space variance.

The initial phase function, $S(x, a_0)$, is obtained from Eq. (6a) by solving

$$\partial_x^2 S(x, a_0) = -m a_0^2 H(a_0) \delta(x, a_0).$$

Once $\{\delta(x, a_0), S(x, a_0)\}$ are known, the initial wave function follows from Madelung's ansatz; see Sec. II A 3.

Each realization starts from $z_0 = 100$ and is integrated until $z = 0$. For the FDM mass two fiducial values, namely $m_1 = 10^{-23}$ eV and $m_2 = 10^{-22}$ eV are analyzed. To guarantee sufficient resolution of $P(k)$ at $z = 0$, the number of uniform spatial grid points is set to $N = 2^{22}$, implying for $L = 100$ Mpc a step size of $\Delta x = 23.8$ pc.

2. Overall evolution of the matter power spectrum

Figure 5 illustrates the evolution of the matter power spectrum for $m_1 = 10^{-23}$ eV, Fig. 5(a), and $m_2 = 10^{-22}$ eV, Fig. 5(b), at various redshifts z. In both panels, the solid black
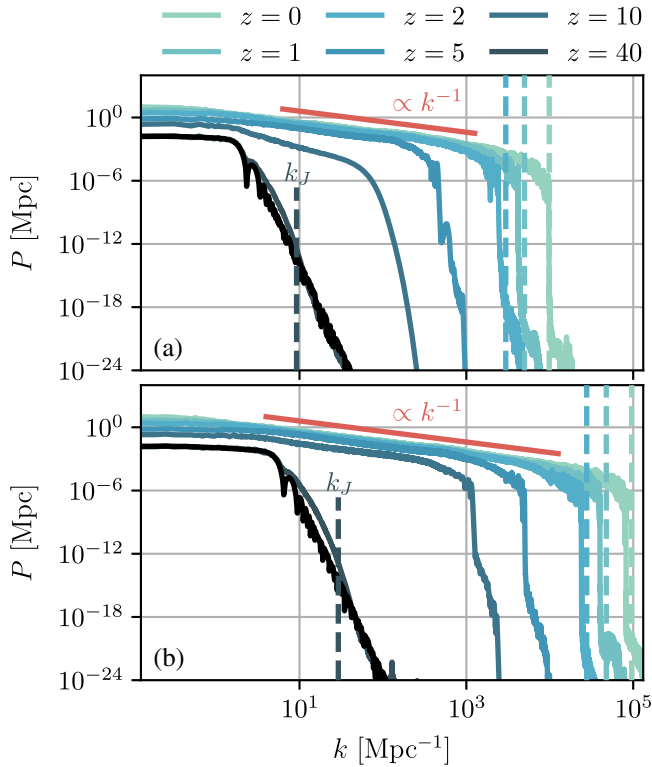
FIG. 5. Evolution of the matter power spectrum $P(k) = \langle |\hat{\delta}_k|^2 \rangle$ inferred from the simulation ensemble specified in Sec. IV A 1 with $m_1 = 10^{-23}$ eV in (a) and $m_2 = 10^{-22}$ eV in (b). The black solid lines show the initial power spectrum, Eq. (30). After small scales pass the time dependent Jeans scale $k_J(a)$, their associated perturbation modes $\hat{\delta}_k$ quickly grow in magnitude and couple to other nonlinearly evolving modes. At late times, this leads to a distinct shape of $P(k)$ with two characteristic regimes: At high k the comoving uncertainty principle induces a sharp power suppression past $k_s(a)$; see Eq. (31) and dashed, vertical lines. By contrast, modes with intermediate values of k, induce a scale free power spectrum with $P(k) \propto 1/k$ cf. Sec. IV A 4.

line represents the linearly rescaled and dimensionally reduced reference spectrum of Eq. (30) from which the initial conditions of each realisation are drawn. It is characterized by a flat, large scale regime quickly transitioning into a steep power law suppression around $k_J(a)$. Its exact functional behavior is encapsulated in the FDM transfer function $T_{\text{FDM}}(k)$.

For both mass parameters the evolution of $P(k)$ may be summarized as follows: Early on, all modes behave linearly, i.e., evolve according to Eq. (8). Recall that complex modes $\hat{\delta}_k$ with $k > k_J(a)$ are stabilized by quantum pressure and are therefore confined to a damped, oscillatory motion with no increase in their magnitude $|\hat{\delta}_k|$. Consequently, as long as all modes evolve linearly, one expects the power spectrum to stay close to its initial shape for $k \gtrsim k_J(a)$. The situation at $z = 40$ recovers this behavior for both mass parameters but is best seen in Fig. 5(b) in which $P(k)$ slowly detaches itself from the power law suppression regime for $k < k_J$. Recall linear FDM modes evolve independent but differently. It is therefore no surprise that the initial shape of $P(k)$ is lost.

As time progresses, k_J proceeds to propagate outward until all modes of interest are destabilized and collapse under their own gravity. It is then that the linearized description of Eq. (8) breaks down and nonlinear mode coupling is expected to set in—the independence of each $\hat{\delta}_k$ is lost. Driven by the focusing, nonlinear interaction, the result is a redistribution of matter power across all nonlinearly evolving perturbation modes. This manifests itself in two observable effects in Figs. 5(a) and 5(b) for all redshifts $z \leq 10$: Firstly, an intermediate coupling regime emerges that is well described by $P(k) \propto k^{-1}$. Secondly, the power suppression regime steepens even further and continues to travel outward, leaving a distinct cutoff in $P(k)$ at high k. Changing the mass parameter influences the transition scale between both regimes.

3. The suppression scale

We recall from Sec. II A 3 that the Jeans length only applies in the linear regime and can therefore not explain the observed transition from matter coupling to suppression. On the other hand, the uncertainty principle remains applicable even under nonlinear evolution. Thus, we adapt the heuristic argument of Sec. II A 3 and again identify the hydrodynamic velocity dispersion as a measure for the velocity uncertainty σ_v, but this time infer the dispersion directly from the simulation. The suppression scale k_s then follows from

$$k_s(a) = \frac{2\pi}{\sigma_x} \approx 2\pi a \frac{m}{\hbar} \sqrt{\langle v^2 \rangle - \langle v \rangle^2} \tag{31}$$

cf. Eq. (7). Figure 5 illustrates its ensemble average $\langle k_s \rangle(a)$ as vertical dashed lines for $z < 5$. The correspondence between $\langle k_s \rangle(a)$ and the true suppression scale is

convincing. We conclude that the small scale evolution remains well explained by the uncertainty principle even in the nonlinear evolution regime.

4. The coupling regime

For scales $k < k_s(a)$ one expects FDM to quickly recover the evolution of cold dark matter (CDM). The observed power-law behavior of $P(k)$ at scales $k_{\mathrm{box}} \ll k < k_s$ should therefore be an intrinsic property of CDM and a consequence of it being collisionless. In fact, by analyzing the CDM evolution in a Lagrangian frame, [69] found recently that the small scale limit of the nonlinear CDM power spectrum in $(1+1)$ dimensions admits the asymptotic expansion,

$$P(k) \sim \frac{\mathcal{C}_0}{k} + \frac{\mathcal{C}_1}{k^3} + \frac{\mathcal{C}_2}{k^5} + \cdots + \frac{\mathcal{C}_n}{k^{2n+1}} \qquad (k \to \infty),$$

with numerical constants $\mathcal{C}_n$ set by the statistical averages of odd derivatives of the Lagrangian displacement field. We refer to [69] for more details. Since higher order terms die out quickly for large enough k, the leading term is sufficient to describe the small scale behavior of $P(k)$ and our low redshift power spectra in Fig. 5 recover the expected $1/k$ scaling. Obviously, the asymptotic behavior is violated once we approach FDM-modified scales, i.e., past $k_s(a)$.

B. Asymptotic (1 + 1)-FDM dynamics

We now shift our attention to the subject of asymptotic dynamics and its equilibrated final $(1+1)$-FDM states. To restrict the complexity of the analysis two simplifications are introduced.

Firstly, artificial, i.e., noncosmologically motivated, initial conditions are employed as these allow us to freely set the degree of spatial localization. This is important since spatially delocalized initial conditions, such as the Gaussian random fields of Sec. IV A, usually come with multiple overdense regions that collapse into multiple, high mass clusters which then undergo a subsequent merger and collision phase. It is these violent, late time events that complicate the dynamics unnecessarily since they drive already relaxed clusters again out of equilibrium, therefore increasing the required integration time to re-relax into the asymptotic state. Moreover, starting from a localized configuration reduces the time to first collapse.

Secondly, to assure swift relaxation times the scale factor, which acts as a coupling constant to the nonlinear interaction, is fixed to $a = 1$. Extensions of our static space time results to the expanding FLRW scenario are deferred to Sec. IV B 5.

1. Simulation setup

More precisely, all simulations reported in this section depart from a Gaussian initial density with zero initial velocity,

$$|\psi(x_3, 0)|^2 \propto e^{-\frac{x_3^2}{2\sigma^2}}, \qquad \mathrm{Arg}[\psi(x_3, 0)] = 0.$$

The standard deviation is chosen as $\sigma = 6k_J^{-1}(1)$ cf. Eq. (9) assuring instability of the entire spectrum of ψ right from the beginning of the evolution. In order to comply with the periodic boundary conditions up to floating point precision, the box size is chosen as $L_3 = 30\sigma \approx 127$ and the numerical study is conducted for both $(1+1)$-SP and the harmonically confined reduction model. In both cases the number of grid points was chosen such that the entire wave function spectrum $|\psi_k|^2$ stays resolved throughout the integration. The integration is stopped some time after Eq. (26) and/or Eq. (28) indicate the completion of the virialization and/or thermalization process.

All data are reported in dimensionless quantities. To get some sense of scale, choosing the canonical FDM mass $m = 10^{-22}$ eV and adopting identical cosmological parameters as in Sec. IV A 1 implies a box size of $L_3 \approx 2.6$ Mpc.

Both reduction models undergo two distinct evolutionary phases—a relaxation period followed by a equilibrated epoch. Their individual phenomenology, however, depends strongly on the nonlocal interaction underlying each $(1+1)$-FDM representation. Below we summarize key aspects of both phases for each reduction model.

2. Relaxation

(1 + 1) Schrödinger-Poisson.—Figure 6 illustrates the relaxation process under $(1+1)$-SP in multiple observables.

For $t \lessgtr 5$ relaxation takes place and is characterized by recurring cycles of (i) infalling matter sheets crossing at the origin, (ii) overshooting the crossing site at $x_3 = L_3/2$, (iii) decelerating until a turn-around radius is hit and finally (iv) recollapsing towards the origin. These cycles do not occur in a strictly sequential manner but are increasingly superposed and thus induce a characteristic spiralization of the phase space distribution in Fig. 6(b). Notice that space regions exist in which multiple inward and outward propagating matter streams coexists simultaneously.

The structure of the early phase space distributions, Figs. 6(a) and 6(b) is qualitatively in good accordance with the evolution of one-dimensional collisionless N-body systems, e.g., [60], and furthermore show the natural signature of phase mixing and (less pronounced) violent relaxation. While phase mixing manifests itself in the ever tighter spiralization of Husimi's distribution, violent relaxation induces a small yet observable increase in the occupied phase space volume. The expansion in k_3-direction is best seen by comparing Figs. 6(a) and 6(b) whereas the white dotted lines in Fig. 6(d) show the spatial expansion. As for collisionless N-body systems, reason for this expansion is the time-dependency of the gravitational potential which dies out quickly after only 1–2 crossing cycles.
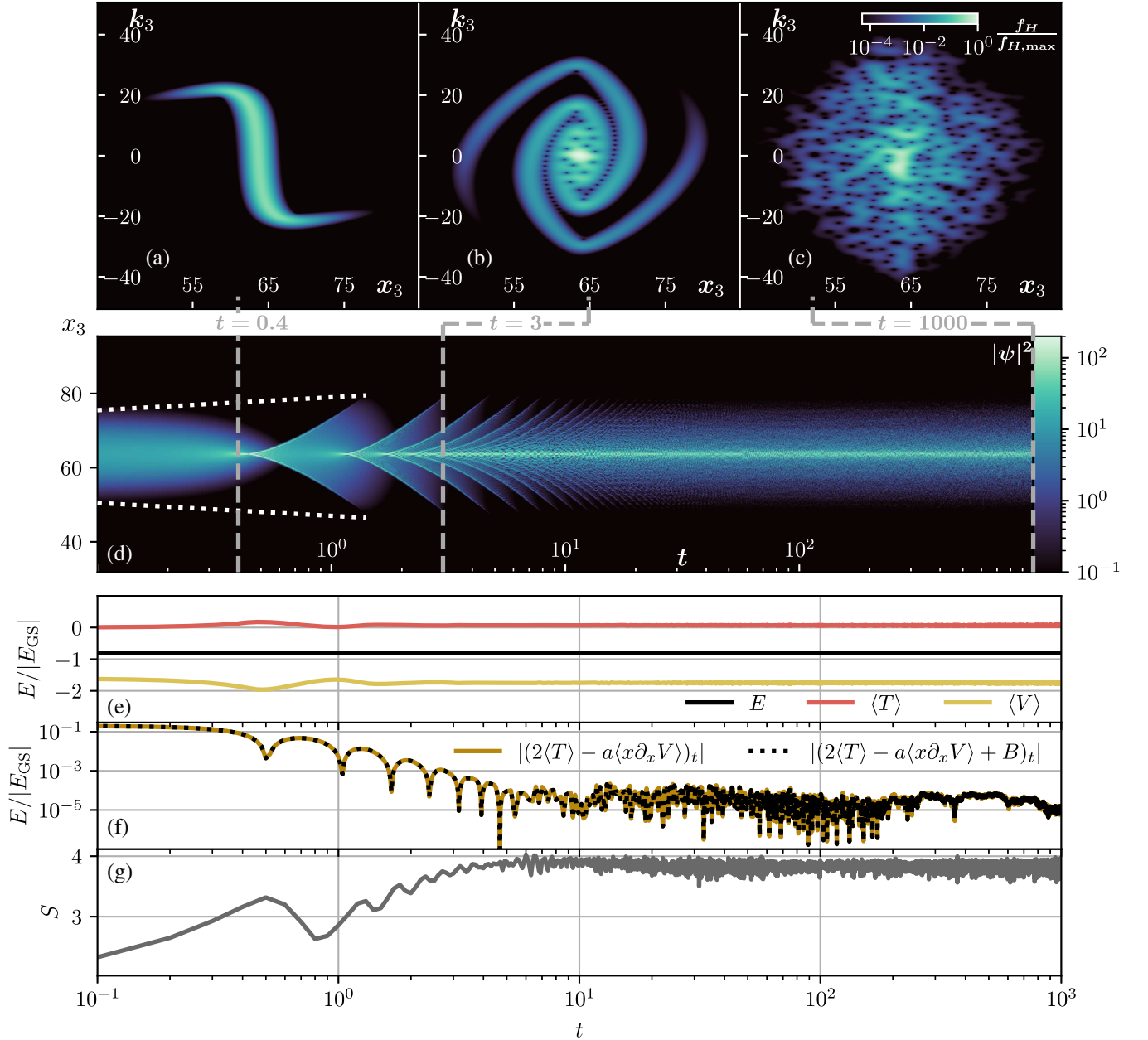
FIG. 6. Relaxation process of an unstable Gaussian density profile under $(1+1)$-SP visualized in multiple observables. (a)–(c) Husimi phase space distribution, Eq. (5), at characteristic stages of the evolution. For all panels a constant smoothing scale of $\sigma_x = 1/\sqrt{2}$ was used assuring equal resolution in the spatial and reciprocal domain. (a) Moment close to shell crossing, i.e., the instance in time when the initially flat phase space sheet is perpendicular to the spatial axis and both inflowing matter streams cross for the first time. (b) After first collapse, a recurring process of partial matter outflow from the crossing site accompanied by a subsequent matter recollapse takes place. The result is a phase space spiral, characteristic for a one-dimensional, collisionless N-body systems; see [60,70]. (c) The coarse-grained Husimi distribution, however, attains a quasistationary form which we associate with the asymptotic, equilibrated system state. (d) Spatiotemporal evolution of the matter density $|\psi|^2$. No qualitatively new features appear in the density past $t \approx 5$ and matter stays organized in a central, high-density core embedded in a halo of fluctuations. White dotted lines visualize the (slight) density expansion in x-space due to violent relaxation (see main text). (e) Energy evolution. The conservation of Eq. (20) is apparent. (f) Assessment of the relaxation process in terms of the quantum virial theorem, Eq. (26). The absolute deviation from Eq. (26) decays quickly until $t \approx 5$ when a lower limit is reached. (g) Assessment of the relaxation process in terms of the proposed maximization of the entropy functional defined in Eq. (28). The entropy evolves in a not strictly monotonically increasing fashion until it saturates at $t \approx 5$. Comparing (f) and (g) reveals that virialization and thermalization occur on the same time scale. All energies were normalized to a $M = L_3$ $(1+1)$-SP ground state.

Each cycle stage is also observable in the energy components in Fig. 6(e), where an increase in the kinetic energy follows from the steep gradient of ψ when matter streams intersect and are therefore maximally localized in space. Once matter flows outward the system is less bound thus increasing the expectation value of the potential energy.

Only 3–4 cycles are required to (i) minimize the absolute deviation from the quantum virial theorem in Fig. 6(f) and (ii) saturate the value of the entropy functional in Fig. 6(g) around $t \lesssim 5$. Thus, the thermalization and virialization time scale are essentially identical and both metrics capture the convergence into the asymptotic state equally well in this example. Furthermore, the boundary term B, Eq. (27), is negligible in this setting as the long interaction range of $G_{\triangle_1}^p$ does not allow ejected matter clumps to propagate till the domain boundaries. Hence ψ and its derivatives persist to be small at $x_3 = 0$.

Strong harmonic confinement.—Figure 7 depicts the situation under strong, harmonic confinement with $\epsilon = 0.01$. Again, a relaxation and quasistationary phase may be identified. Their respective duration, however, is opposite to $(1 + 1)$-SP.

During relaxation, i.e., when $t \lesssim 950$, the system exhibits a short phase of matter emission in response to the violent collapse of the initial conditions, best seen in spatiotemporal evolution of $|\psi|^2$ in Fig. 7(d), around $t \approx 2$. There, multiple, stable density excitations of various masses depart from the position of first collapse, propagate outward, overcome the central gravitational potential at $x_3 = L_3/2$ and proceed to travel towards the domain boundaries as unbound excitations. Closer inspection reveals the non-diffusive, form invariant nature of these excitations—solitary waves.

The remaining part of the relaxation phase may then be summarized as a series of inelastic solitary wave encounters, akin to Sec. II B 4 b. Recall during these encounters matter and energy is transferred from the low to high mass solitary wave.

Once the kinetic energy of a low mass stationary excitation is insufficient to escape the gravitational well of a high mass solitary wave, a merger takes place, Fig. 7(b). The matter of both waves then reorganizes into a single gravitationally bound structure while expelling excess energy in form of small scale background fluctuations—the signature of gravitational cooling, [30]. These become visible as completely delocalized background in which all solitary waves are embedded.

As the gas of solitary excitations continues to rarefy, the background grows in magnitude up to $\mathcal{O}(1)$ until all stationary states have been consumed by a single high mass solitary wave; see Fig. 7(c). At this point the asymptotic, relaxed system configuration is reached.

Inspection of the virialization theorem, Fig. 7(f), and the entropy evolution, Fig. 7(g), reveal that both observables capture the relaxation process equally well and report virialization or thermalization around $t \approx 950$ respectively. Importantly, since the dynamics spans over the entire domain, the boundary term in Eq. (27) cannot be neglected. In fact, a naive application of the quantum virial theorem omitting the boundary term would suggest a departure from the equilibrium state.

Let us close this section by mentioning two imperfections of the reported data. Firstly, $|\psi|^2$ experiences an unphysical symmetry breaking around $x_3 = L_3/2$ in its evolution past $t = 100$ being induced by small numerical errors. The same symmetry breaking is also apparent in Fig. 6 for $(1 + 1)$-SP. Assessing the situation in more detail reveals an absolute momentum drift of $\langle p \rangle = 10^{-3}$. Given the long integration time and the high degree of mobility seen in $|\psi|^2$, we find this momentum conservation violation still to be acceptable.

Secondly, the evolution of the virial theorem experiences unphysical jumps when significant amounts of matter travels across the domain boundary, e.g., at $t \approx 250$. These upticks originate from sudden changes in the boundary term, Eq. (27), being insufficiently resolved in the continuous time averaging of Eq. (26). Clearly, increasing the sampling rate of ψ around these events mediates this problem. However, one cannot anticipate *a priori* when matter flows past the periodic boundary, making the nonstationary virial theorem cumbersome to work with in practice.

3. Final states

(1 + 1) Schrödinger-Poisson.—Past $t \approx 5$, one finds the system in a quasistationary configuration. We coin the attained state quasistationary since the entire matter density still undergoes significant time-dependent variation yet does not produce qualitatively new features in the spatiotemporal evolution of $|\psi|^2$ cf. Fig. 6(d). What remains is a circular phase space distribution comprised of a high density core and halo of fluctuations surrounding it, see Fig. 6(b). One may think of this phase space distribution as the result of smoothing out the fine-grained filament structure of an ever tighter spiraled distribution on the scale of Heisenberg's uncertainty principle $\sigma_x \sigma_k = \frac{1}{2}$.

To answer whether the core coincides with a $(1 + 1)$-SP ground state, we consider the mean spectral composition of $|\psi_{k_3}|^2$ obtained by averaging 100 quasistationary wave functions past $t > 990$, i.e., well inside the relaxed epoch. Figure 8(a) compares the result with the spectrum of a $(1 + 1)$-SP ground state of maximum mass $M = L_3$. The ground states were generated independently, as discussed in Sec. II B 4. Evidently, no convincing agreement is achieved, and the time asymptotic spectrum appears generally too broad for any viable ground state with $M < L_3$. Changing the width and location of the averaging time interval does not yield any improvements.
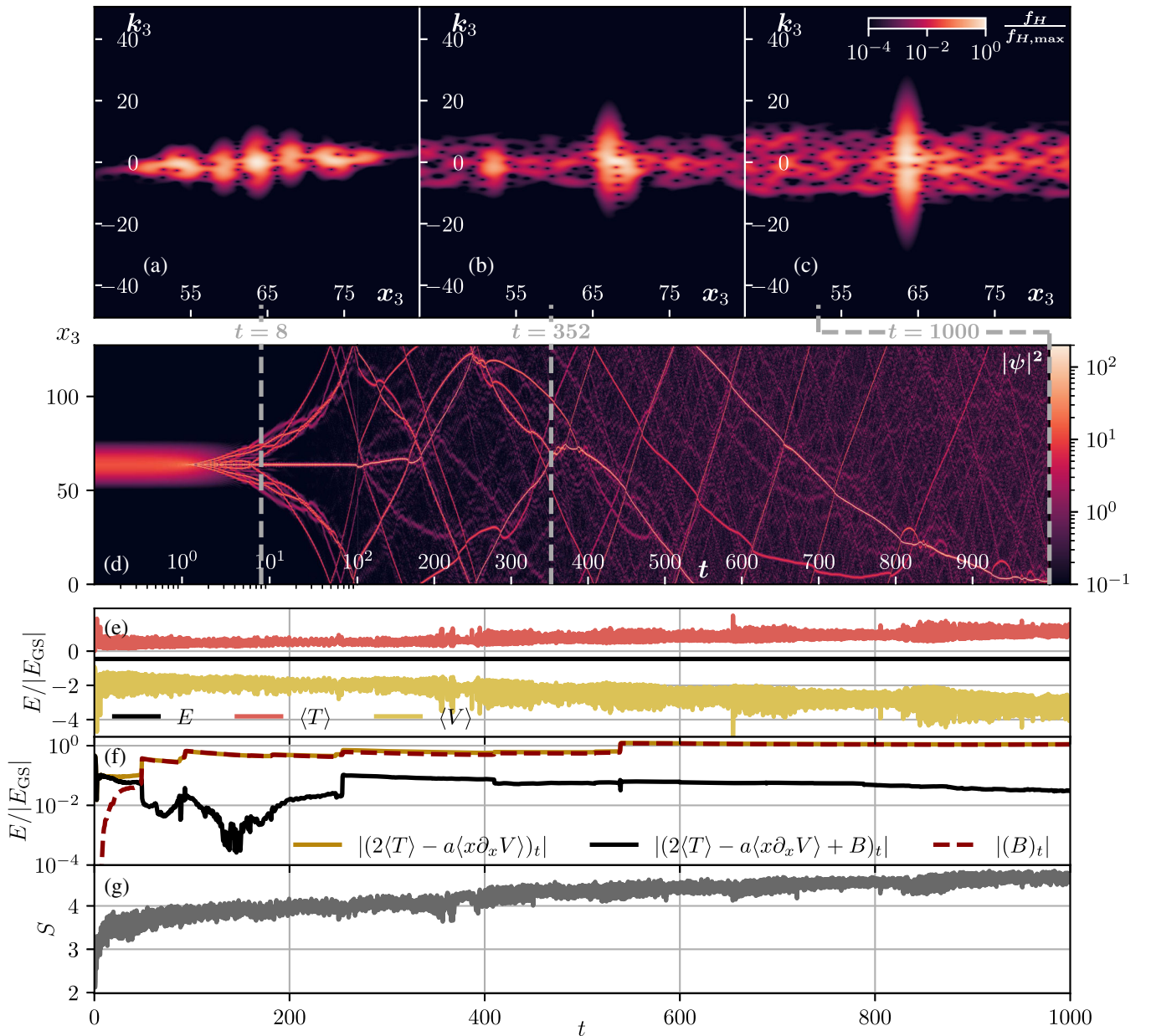
FIG. 7.   Relaxation process of an unstable Gaussian density profile under strong confinement, i.e., $\epsilon = 0.01$, in multiple observables. (d) Spatiotemporal evolution of $|\psi|^2$. One finds a stark contrast in the evolution of the strongly confined reduction model compared to the unconfined scenario in Fig. 6. In particular, nondiffusive, stable excitations are ejected from the collapse sight. Their bulk velocity is sufficient to leave the small interaction range of U_{conf}^p and thus propagate freely through the entire domain without recollapsing to the domain center. The subsequent evolution may then be summarized as series of inelastic solitary wave interactions involving different mass ratios and during which high mass excitations slowly consume small mass excitations until a final solitary wave persists at $t = 1000$. As a byproduct a completely delocalized fluctuation background emerges that increases in magnitude up to $\mathcal{O}(1)$. (a)–(c) Spatially recentered Husimi distributions, see Eq. (5). σ_x chosen as in Fig. 6. (a) Contrary to $(1 + 1)$-SP no phase space spiral develops. Instead circular, solitary excitations manage to leave the central gravitational potential. (b) Example of a excitation merger taking place in a spatially delocalized, fluctuating background. (c) Quasistationary, final state after all solitary waves merged into a single high mass stationary configuration. (e) Energy evolution. Again total energy conservation is apparent. Variations in the potential and kinetic energy originate from solitary interactions and the associate expel of excess energy during their mergers. (f) Deviation from the virial theorem in Eq. (26). Note without the boundary term the system would depart from virial equilibrium. All energies in (e) and (f) are normalized to the ground state shown in Fig. 9. (g) Entropy evolution cf. Eq. (28). Thermalization takes significantly longer compared to $(1 + 1)$-SP and is only completed at $t \approx 900$ when all solitary excitations have been consumed. The thermalization time is again comparable to the virialization time.
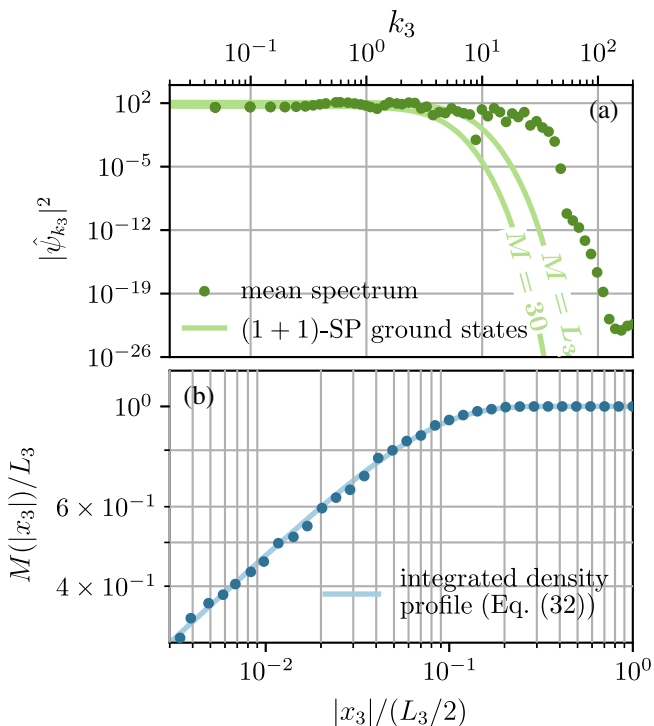
FIG. 8. Analysis of the quasistationary state of $(1+1)$-SP extracted from Fig. 6. (a) Comparison of the mean wave function spectrum obtained by averaging 100 wave functions past $t = 990$ alongside two $(1+1)$-SP ground state spectra. The latter were generated by means of a gradient descent, Sec. II B 4. The poor correspondence between the spectra suggests that the minimal energy solutions to $(1+1)$-SP does not act as dynamical attractors in the evolution. (b) Integrated and normalized FDM density obtained from $|\psi|^2$ at $t = 1000$ after radial averaging. One finds good correspondence with the halo density model of Eq. (32) with $\gamma \approx 0.62$.

We conclude although $(1+1)$-SP realizes a cored density profile, this core is not a ground state configuration of its Hamiltonian—a qualitative difference to $(3+1)$-SP. Nevertheless, there is still something to be learned about the obtained long term density distribution. The complementary, classical view point of Sec. II A 2 b suggests to compare the results of $(1+1)$-SP with predictions for one-dimensional, collisionless N-body systems, in particular density profiles for dark matter haloes.

For the situation at hand [60] observed how phase mixing and violent relaxation drives such system towards power-law densities $\rho(x_3) \propto |x_3|^{-\gamma}$ with $\gamma \simeq 0.5$. Inspired by Einasto's profile, [71], the authors of [72] extended this halo model by an exponential suppression factor dominant past a cutoff radius r_0. Following this argumentation, one expects

$$\rho(x_3) \propto |x_3|^{-\gamma} \exp\left(-\left(\frac{|x_3|}{r_0}\right)^{2-\gamma}\right) \quad (32)$$

for a $d = 1$ dimensional CDM halo located at $x_3 = 0$.

In accordance with [44], we consider the integrated and normalized halo mass $M(|x_3|)/L = \frac{2}{L}\int_0^{|x_3|}\mathrm{d}x_3\rho(x_3)$ instead of $\rho(x_3)$, thus sparing us to choose a particular value of the smoothing scale σ_x—recall the necessity of smoothing to obtain a satisfactory Vlasov-Schrödinger correspondence. Figure 8(b) depicts how this halo model compares to the simulated $(1+1)$-SP density at $t = 1000$. We observe a satisfactory correspondence with the fit model of Eq. (32) at $\gamma \approx 0.62$. Better results are achievable in the limit $\hbar \to 0$; see [44].

(1 + 1) Strong harmonic confinement.—Repeating the spectral analysis in Fig. 9(a) yields convincing accordance between the mean wave function spectrum and a strongly confined ground state of mass $M = 48$. The remaining spectral disturbances which were not completely suppressed by the time-averaging are confined to $|k_3| < 10$. Comparison with the quasistationary phase space distribution in Fig. 7(c) shows they originate from the delocalized background oscillations.

We conclude that the inelastic excitation dynamics experienced during relaxation does in fact drive the system towards a single high mass ground state. One may regard the minimal energy solution as the fixed point in the long term evolution under strong confinement—a result in stark contrast to our observations for $(1+1)$-SP but qualitatively close to the $(3+1)$-FDM phenomenology.

The halo matter undergoes spatial variation which diminish after averaging multiple radial density profiles in the same time window used for Fig. 9(a). The resulting mean density of Fig. 9(b) then indicates a power law halo profile outside the core consistent with the decay behavior of the numerically obtained $(1+1)$-SP halo. This is to be expected, since there is no reason to assume a strongly confined, one-dimensional halo organizes into a canonical $1/|x_3|^3$-NFW profile [31]. Intuitively, the behavior of a dark matter halo should be influenced by (i) the interaction in the far field and (ii) dimension dependent effects such as geometrical dilution.

To substantiate this claim, we impose spherical symmetry to the full-fledged problem in Eq. (1) and adopt the regularization approach of [73]. The choice of spherical symmetry presents yet another reduction of dimensionality to $(1+1)$. Doing so allows us to implement the same $1/r$-far field behavior as in our confinement model while making the density dilution in radial direction manifest. Excess matter radiated away during the relaxation process is suppressed with a complex absorbing potential situated at the domain boundary, e.g., [27,29]. We refer to Fig. 10 for the relaxed, mean density profile obtained from a ensemble of $\mathcal{N} = 20$ Gaussian initial conditions of various masses. Application of the scaling symmetry, Eq. (21), allows us to rescale each realization to a common peak density. Evidently, matter not included in the ground state core now organizes into a NFW profile.
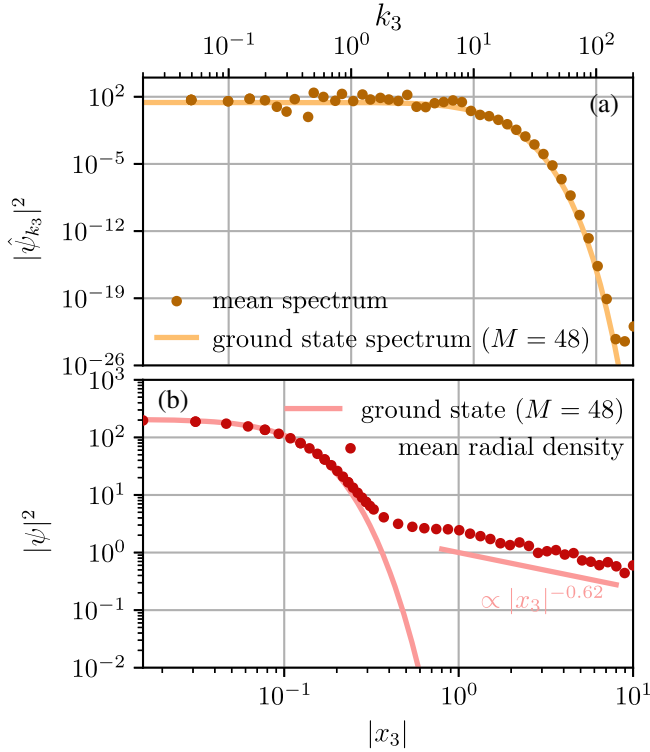
FIG. 9. Analysis of the quasistationary state under strong harmonic confinement with $\epsilon = 0.01$ extracted from Fig. 6. (a) Comparison of the mean wave function spectrum obtained by averaging 100 wave functions past $t = 990$ alongside the best matching ground state of mass $M = 48$ cf. Fig. 2. Also note that the remaining deviations from the ground state spectrum are confined to $|k_3| < 10$—exactly the wave number regime in which the delocalized background density is situated in Fig. 7. (b) Radially and temporally averaged density. Time averaging as in (a). Again a clear distinction between ground state core and adjacent halo density can be made. Moreover, the halo surrounding the core indicates the same power law scaling found for the $(1 + 1)$-SP halo of Fig. 8.

4. Control of self-organization processes

The foregoing discussion highlighted the superiority of the transversal confinement model in mapping the $(3 + 1)$-FDM phenomenology to one-dimensional analogues—while both models indicate reasonable accordance with classical predictions for the outer halo density, it is only under confinement that the equilibrated state evolves towards a ground state core.

In fact, the observed self-organization principle of $(1 + 1)$-FDM under strong confinement is not new. The author of [74] showed how for a class of focusing, *local* nonlinearities of the NLSE perturbed uniform initial conditions have a single soliton as dynamical attractor. More precisely, the perturbed initial conditions develop a number of small mass solitons which subsequently merge into a single high-mass soliton at late times. This phenomenon was coined *soliton turbulence,* and it was argued it is
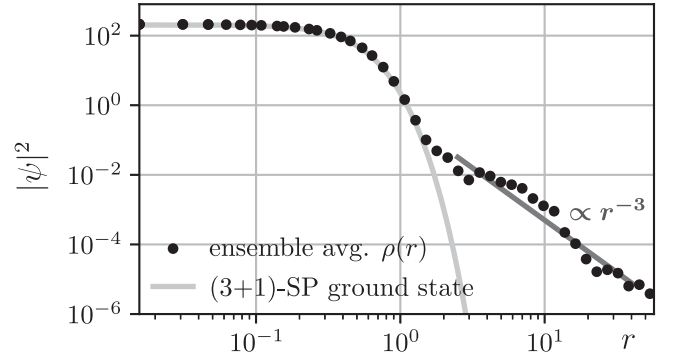

FIG. 10. Ensemble averaged radial density deduced from $\mathcal{N} = 20$ realizations of different mass, initial Gaussians. The integration was performed under the assumption of spherical symmetry. Notice that in addition to the ground state ("solitonic") core, the remaining matter organizes into a power law halo, $\rho \propto r^\gamma$, at larger radii. A fit yields $\gamma \approx -3.1$. Within the limits of accuracy of our data, we deem this to be consistent with the asymptotic behavior of the NFW halo density, i.e., $\rho \sim r^{-3}$, shown as gray solid line.

"thermodynamically favorable" for the system to develop in this particular way. The authors of [75] later put these findings on more theoretical grounds by developing a statistical theory around a mean-field approximation of the nonlinear Hamiltonian obeying a maximum entropy principle.

The problem of *nonlocal* interactions was considered in the context of nonlinear optics by [5]. Numerical and analytical arguments showed that the dynamics is mainly driven by the ratio between the interaction range R and the soliton size σ: if the interaction range is too large, matter far away from a potential soliton, but still within interaction range, contributes significantly to the convolution integral. Consequently, the delicate potential required to form a soliton gets averaged out by the surrounding fluctuations. Hence, one expect soliton-turbulence-like behavior for $R \ll \sigma$. In case of $R \geq \sigma$, the system organized into a "spatially localized incoherent structure" coined *incoherent soliton*. Their results resemble our findings for the quasistationary state of $(1 + 1)$-SP.

A limit not yet discussed, is the weak confinement regime, i.e., $\epsilon \to \infty$. It is intuitively clear that in this case the interaction kernel $U_{\text{conf}}^{\text{p}}$ should approach $G_{\triangle_1}^{\text{p}}$. A more careful analysis shows

$$U_{\text{conf}}^{\text{p}}(x_3, x_3') \sim \frac{1}{2\pi\epsilon^2} G_{\triangle_1}^{\text{p}}(x_3, x_3') \quad (\epsilon \to \infty).$$

Increasing ϵ should therefore allow us to observe a transition from the soliton to incoherent soliton turbulence regime. To keep relaxation times comparable we also substitute $a \to 2\pi\epsilon^2 a$ so that the effective nonlinear coupling stays unity.
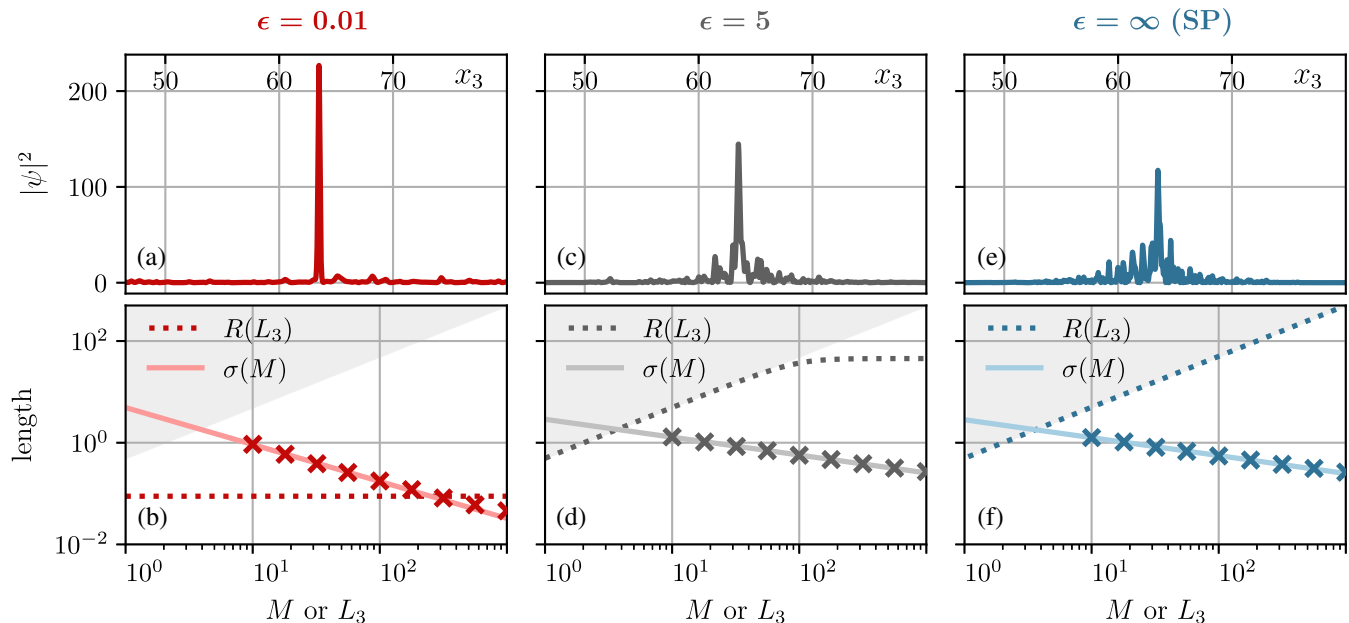
FIG. 11. Overview of asymptotic states as a function of the confinement parameter ϵ. From left to right, we have (a)–(b) analyzing the strong confinement limit ($\epsilon = 10^{-2}$), (c)–(d) assessing the weak confinement regime ($\epsilon = 5$) and (e)–(f) evaluating the uniform reduction scenario in the limit $\epsilon \to \infty$, i.e., $(1+1)$-SP. Upper panels: Snapshot of the attained quasistationary states. Lower panels: Comparison of the interaction range $R(L_3)$, Eq. (17), and the soliton size $\sigma(M)$, Eq. (25). Crosses denote soliton sizes directly inferred from the gradient descent of various mass solitons cf. Fig. 4. Solitons with sizes inside the gray shaded area do not exist as they violate periodic boundary conditions. For $\epsilon > 1$, we find a transition away from turbulent soliton dynamics toward a "incoherent soliton" configuration, i.e., a highly fluctuating state comprised of many density maxima beating against each other in real space. As argued in [5], this regime is entered once the interaction range $R(L_3)$ is significantly larger than the soliton size $\sigma(M)$. Even in the best case scenario for (d) and (f), i.e., when a soliton of maximal size could form, one still finds $\sigma_{\max}/R(L_3 \approx 127) < 0.1$—far outside the soliton regime. By contrast, the strong confinement scenario of Fig. 9, or equivalently (a), realizes $\sigma(M = 48)/R(L_3 \approx 127) > 1$ and is therefore well inside the soliton regime.

Figure 11 compares the asymptotic state obtained under strong, weak, and no confinement alongside the respective interaction range $R(L)$, Eq. (17), and soliton extent $\sigma(M)$, Eq. (25).

We find confinement parameters larger than unity to quickly approach quasistationary states comprised of many density maxima beating against each other around the origin. These configurations are qualitatively identical to the $(1+1)$-SP case. Comparing the maximal, boundary condition compatible soliton size $\sigma_{\max}$ with the interaction range $R(L_3)$ at the chosen domain size $L_3 \approx 127$ shows $\sigma/R < 0.1$, which according to [5] implies "incoherent soliton" dynamics, and in particular no solitonic attractor. On the other hand comparing both length scales for $\epsilon = 0.01$, where a $M = 48$ soliton is formed, we have $\sigma/R > 1$, consistent with the soliton turbulence regime.

5. Space-time expansion

The foregoing results of Sec. IV B 4 allow us to extend the discussion to nonstatic background cosmologies. We first note that the interaction range, as defined in Eq. (17), is independent of the nonlinear coupling constant. The soliton size $\sigma(M)$, on the other hand, is. This is intuitively clear: Decreasing the nonlinear coupling increases the importance of the diffusive character of kinetic term in the Hamiltonian—we approach a free Schrödinger equation. Hence, the radius at which the focusing nature of the nonlinearity balances the kinetic term is expected to increase as well.

Under strong confinement cf. Fig. 11(b) an expanding background cosmology would therefore drive the system even further into the soliton turbulence regime $\sigma \gg R(L)$.

Without confinement cf. Fig. 11(f) the typical increase of $\sigma(M)$ experienced by starting from reasonable initial redshifts, say $z = 100$, is insufficient to realize $\sigma_{\max} \approx R(L)$, around which a transition to the soliton turbulence regime should occur. Note that here $\sigma_{\max} > R(L)$ is never achievable as it would violate the periodic boundary conditions. That said, allowing for a time dependent coupling constant has, aside from numerical implications, also influence on the relaxation time. Preliminary analysis shows that although the strong confinement scenario including a Friedmann-Lemaître-Robertson-Walker (FLRW) background does trend towards a ground state ("solitonic") spectrum, relaxation is not completed at $z = 0$. Figure 12 illustrates this result. A full-fledged analysis of the expanding model is left to future work.
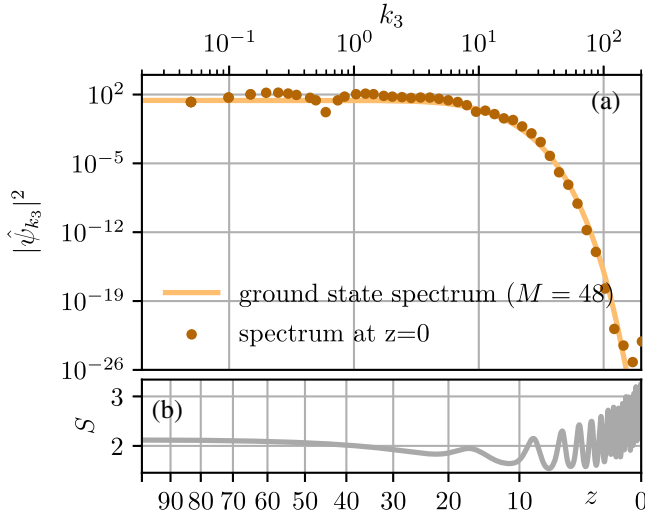
FIG. 12. Strong confinement model with $\epsilon = 0.01$ undergoing collapse in a background cosmology as in Sec. IV A 1. (a) Final wave function spectrum at $z = 0$ together with the same $M = 48$ ground state of Fig. 9. (b) Entropy evolution. It is evident that relaxation is not completed at $z = 0$.

V. CONCLUSION

Purpose of this work was to conduct an extensive numerical study on the applicability of the fuzzy dark matter (FDM) model in one spatial dimension. Particular emphasis was put on (i) the properties of the system's long term evolution, (ii) the structure of the relaxed, asymptotic system state and how it compares to the core-halo structure of $(3 + 1)$-FDM, as well as (iii) which model parameters may be used to control its phenomenology. To this end, we derived two distinct one-dimensional FDM models by either allowing for a complete delocalization of matter in the transversal plane, $(1 + 1)$-SP, or by confining all matter along one spatial direction. While both models realize long range interactions free of singularities, it is only under strong confinement that the nonlocal interaction recovers the desired $-1/r$ interaction at large distances.

We proceeded to investigate the mean cosmic structure growth in an ensemble of FDM-only, flat FLRW-universes obeying $(1 + 1)$-SP and starting from cosmological initial conditions. By following the evolution of the matter power spectrum until present time, two distinct spectral ranges were identified: firstly, a suppression range, in which the power spectrum is smoothed out by the uncertainty principle. Secondly, a coupling regime, where the redistribution of matter across nonlinearly evolving modes leads to a scale-free spectrum consistent with considerations for $(1 + 1)$-CDM. The transition scale from coupling to suppression followed by a self-consistent application of the uncertainty principle.

The analysis of the asymptotic system state was conducted under simplifying assumptions, i.e., a static background cosmology and spatially localized initial conditions.

Our study suggests that $(1 + 1)$-SP relies on violent relaxation and phase mixing to approach its equilibrated, i.e., thermalized and virialized, system state. Although the realized asymptotic configuration does form a core-halo structure, the central core cannot be identified with the ground state solution of the $(1 + 1)$-SP Hamiltonian—a stark contrast to $(3 + 1)$-FDM for which the minimum energy solution acts as dynamical attractor in the long term evolution. The halo density, on the other hand, was found to be consistent with structure of one-dimensional CDM halos.

By contrast, the evolution under strong confinement favours the $(3 + 1)$-FDM typical relaxation mechanism of gravitational cooling. Ultimately, the evolution then converges into a virialized and thermalized system state comprised of a single high-mass ground state solution embedded in a delocalized fluctuation background that emerges from a series of inelastic ground state interactions. The analysis of the halo density suggested identical CDM-like behavior as for $(1 + 1)$-SP. We conclude that under the chosen simulation conditions the strongly confined reduction model is superior in mapping the three-dimensional phenomenology to one spatial dimension.

To understand the reason for the qualitative difference between the asymptotic behavior of $(1 + 1)$-SP and the confinement model, we investigated the weak confinement limit of our reduction. In accordance with arguments from nonlinear optics, see e.g., [5], we found the system to converge towards a high-mass ground state if the effective interaction range is (considerably) smaller than the spatial extent of the ground state. For $(1 + 1)$-SP and arbitrary but fixed coupling constant, no ground state exists that satisfies this condition. It is for this reason that we conjectured our static space-time analysis remains valid even for nontrivial background cosmologies. Although our work focused on an interaction kernel that resembles Newtonian gravity, results from nonlinear optics suggest that the dependence of the asymptotic state on the interaction range is a property also applicable for other long range potentials. For instance, the authors of [5] implemented a Gaussian interaction kernel in Eq. (13), while [6] employed a screened Poisson equation as field equation. The latter approach implies an exponentially decaying Greens function.

Our work may be extended in multiple regards. From a physical perspective, a full-fledged investigation of cosmological initial conditions in various cosmological expansion models is still pending, and the phenomenology under strong confinement is presumably not exhausted by our discussion. In this context, we mention the properties of the delocalized fluctuation background as it may be possible to understand it as an ensemble of small scale plane waves obeying a dispersion relation akin to Bogoliubov's excitation spectrum for Bose-Einstein condensates [4,76].

Moreover, additional conceptional optimizations of our confinement approach are worth exploring. For instance, our work only focused on a global, statically set

confinement parameter. However, incorporating the confinement ansatz directly into SP's generating action is expected to yield additional information on the spatiotemporal evolution of the confinement strength itself, thereby allowing it to be set self-consistently and dependent on the wave function evolution [50].

We also remark on our ongoing effort to optimize our numerical approach by means of a more efficient basis-function method or splitting schemes with intrinsic error estimates. With this we hope to (i) achieve a fully adaptive spatiotemporal grid that is sensitive to nonlinear evolution and (ii) pave the way for a higher dimensional analysis. The latter should allow the investigation of additional relaxation channels unique to FDM, especially the emission of quantized vortices that may play an important role for the asymptotic evolution on top of gravitational cooling.

Altogether, we hope that our investigation will lead to a better cross-fertilization, see also [11], between cosmology, statistical mechanics [37,38], nonlinear dynamics [77,78], nonlinear wave optics [5–8], and the quantum evolution of, e.g., Bose-Einstein condensates [79–85], with the scope to obtain further insight into the complex dynamics of the SP model and to search for possible laboratory experiments for the implementation and analogue simulation of FDM models.

APPENDIX: CONVERGENCE AND STABILITY

Let us now give a numerical justification for the accuracy and stability claims mentioned in Sec. III C. To this end, we conduct a convergence and stability study for the simulation scenarios of Sec. IV A 1 (delocalized random field including space-time expansion) and Sec. IV B 1 (unstable Gaussian initial conditions in a static background cosmology).

The authors are not aware of a general analytical result in any of these cases. Thus, we compute a reference solution ψ_{ref} on a fine spatiotemporal grid $\{N_{\mathrm{ref}}, \Delta t_{\mathrm{ref}}\}$ and measure the error of ψ relative to ψ_{ref} via $\Delta \epsilon = \|\psi_{\mathrm{ref}} - \psi\|_2 / \|\psi_{\mathrm{ref}}\|_2$. Note the error $\Delta \epsilon$ is a function of N, Δt and integration time t. Since the results are qualitatively identical for $(1 + 1)$-SP and the confinement model we only report data for the former.

We begin with the cosmological simulation scenario of Sec. IV A, i.e., a random field evolving in a dynamic FLRW background. Figure 13 depicts the dependence of the numerical error as a function of the spatiotemporal grid parameters $\{N, \Delta t\}$ relative to the reference grid $\Delta t_{\mathrm{ref}} = 10^{-5}$ and $N_{\mathrm{ref}} = 2^{22}$ (the white cells). The grid parameters of Sec. IV A are marked with a black cross. To assure comparability, all 56 $\{N, \Delta t\}$ combinations are initialized
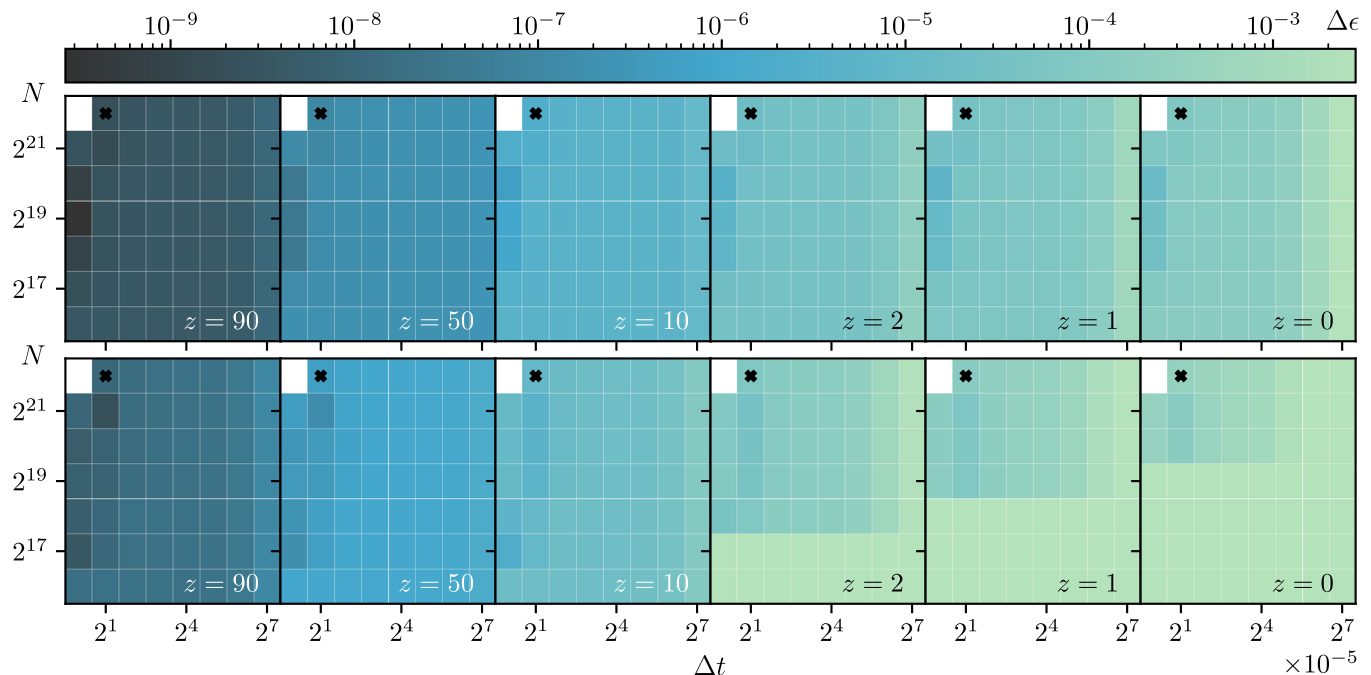

FIG. 13. Evolution of the relative error $\Delta \epsilon$ as a function of the spatiotemporal grid. The convergence study adopts the initial conditions and parameters of Sec. IV A 1 using $m_1 = 10^{-23}$ eV in the first row and $m_2 = 10^{-22}$ eV in the second row. Space-time expansion is turned on. The white cells corresponds to the numerical reference solution ψ_{ref} relative to which $\Delta \epsilon$ is computed. The black cross represents the spatiotemporal grid used for Fig. 5.
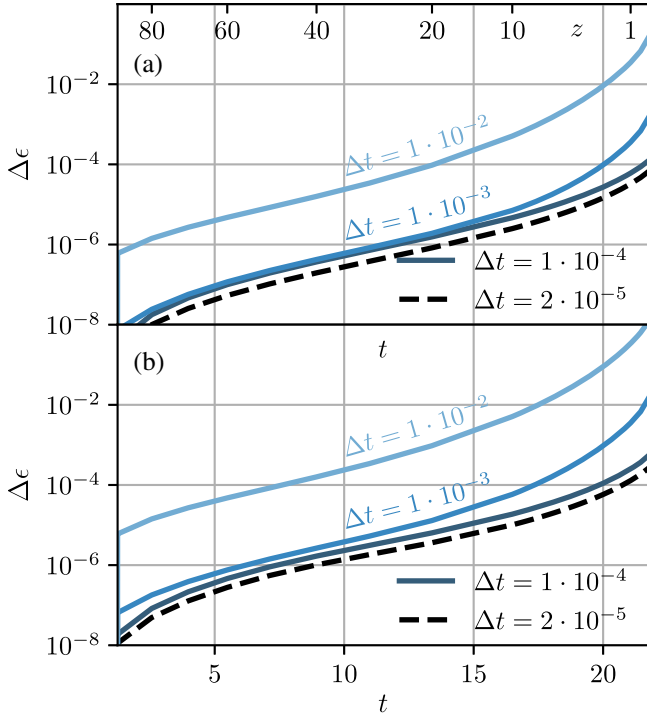
FIG. 14.   Evolution of the numerical error $\Delta\epsilon$ as a function of the integration time. The convergence study adopts the initial conditions and parameters of Sec. IV A 1 with $m_1 = 10^{-23}$ eV in (a) and $m_2 = 10^{-22}$ eV in (b). Space-time expansion $a(t)$ is turned on. The space-time grid of Sec. IV A corresponds to the black, dashed line.

with every N/N_{ref} point of the same reference Gaussian random field $\delta(x)$.

In the $m = m_1$ case, we find a high degree of uniformity in N at fixed Δt throughout the integration. This is the result of the spectral accuracy of the employed spatial discretization. Variations of the relative error $\Delta\epsilon$ in N at $\Delta t = 1$–2×10^{-5} are common once we reach the convergence plateau but may also be induced by a lack of fidelity close to the reference solution. More pronounced is the loss of accuracy in Δt direction (at any considered N), and we conclude the overall inaccuracy is dominated by the temporal error. Solutions $\Delta t \leq 8 \times 10^{-5}$ can be considered as converged.

The situation for the $m = m_2$ scenario is qualitatively identical with an additional caveat at low red shifts. Here, spatial grids with $N < 2^{20}$ proof to be insufficient to resolve the entire spectrum of $|\hat{\psi}_{k_3}|$. In this case spatiotemporal grids with $N > 2^{20}$ and $\Delta t \leq 8 \times 10^{-5}$ are deemed sufficient to achieve convergence.

Concerning temporal accuracy and overall stability, we refer to Fig. 14 which evaluates the time dependence of the numerical error for various time increments Δt at fixed
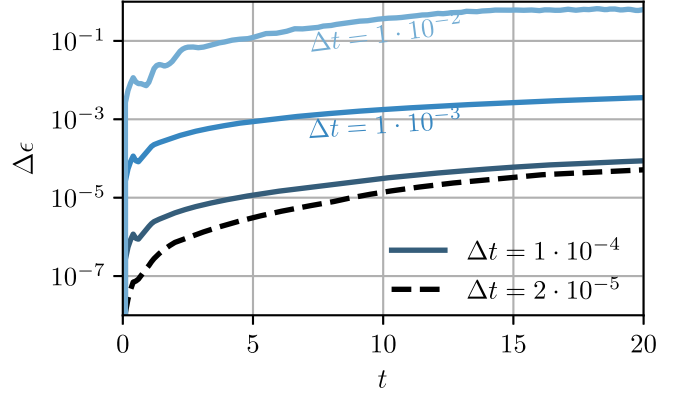

FIG. 15.   Evolution of the numerical error $\Delta\epsilon$ as a function of the integration time. The convergence study adopts the initial conditions and parameters of Sec. IV B 1. Space-time expansion is turned off, i.e., $a = 1$. The space-time grid of Sec. IV B corresponds to the black, dashed line.

$N = N_{\mathrm{ref}} = 2^{22}$. The reference solution is identical to the one used in Fig. 13 and the spatiotemporal grid of Sec. IV A is depicted as black, dashed line.

Evidently, allowing for an dynamic cosmological background yields a numerical error that evolves roughly exponentially. Nevertheless, errors are still of acceptable size at present time which is why we deem our numerical treatment of the nonautonomous Hamiltonian as acceptable for the purposes of this work. Decreasing the time step beyond $\Delta t < 10^{-4}$ results in no significant gain in accuracy. Note that the nonconverged time steps, i.e., $\Delta t = 10^{-2}, 10^{-3}$ approach the convergence plateau with roughly quadratic speed. This can be inferred from their relative offset which evaluates to about 2 orders of magnitude and is expected given that Strang splitting cf. Sec. III B is second order accurate in time.

Let us contrast the error evolution of the fully cosmological case with the static simulation conditions of Sec. IV B cf. Fig. 15. Here, the smaller dimensionless box size allows us to reduce the number of spatial grid points required to fully resolve the spectrum of ψ. This in turn makes a smaller reference time increment possible. Figure 15 therefore uses a reference grid with $\Delta t_{\mathrm{ref}} = 10^{-6}$ and $N_{\mathrm{ref}} = 2^{13}$. Again, the grid parameters used in Sec. IV B correspond to the black, dashed line.

As for the cosmological evolution, quadratic accuracy is achieved for nonconverged time steps approaching the plateau. A notable difference, however, is the growth behavior of $\Delta\epsilon(t)$ which only evolves linearly in time if the scale factor remains static. It is for this reason that we can extend the integration time up to $t = 1000$ cf. Sec. II C without losing reliability of our data.

[1] A. L. Fetter and J. D. Walecka, *Quantum Theory of Many-Particle Systems* (Dover Publications, New York, 2003).

[2] G. D. Mahan, *Many Particle Physics (Physics of Solids and Liquids)* (Kluwer Academic/Plenum Publishers, New York, 2000).

[3] F. Dalfovo, S. Giorgini, L. P. Pitaevskii, and S. Stringari, Theory of Bose-Einstein condensation in trapped gases, Rev. Mod. Phys. **71,** 463 (1999).

[4] L. P. Pitaevskii and S. Stringari, *Bose-Einstein Condensation and Superfluidity* (Oxford University Press, Oxford, 2016).

[5] A. Picozzi and J. Garnier, Incoherent Soliton Turbulence in Nonlocal Nonlinear Media, Phys. Rev. Lett. **107,** 233901 (2011).

[6] R. Bekenstein, R. Schley, M. Mutzafi, C. Rotschild, and M. Segev, Optical simulations of gravitational effects in the Newton–Schrödinger system, Nat. Phys. **11,** 872 (2015).

[7] T. Roger, C. Maitland, K. Wilson, N. Westerberg, D. Vocke, E. M. Wright, and D. Faccio, Optical analogues of the Newton–Schrödinger equation and boson star evolution, Nat. Commun. **7,** 13492 (2016).

[8] A. Navarrete, A. Paredes, J. R. Salgueiro, and H. Michinel, Spatial solitons in thermo-optical media from the nonlinear Schrödinger-Poisson equation and dark-matter analogs, Phys. Rev. A **95,** 013844 (2017).

[9] L. Diósi, Gravitation and quantum-mechanical localization of macro-objects, Phys. Lett. **105A,** 199 (1984).

[10] R. Ruffini and S. Bonazzola, Systems of self-gravitating particles in general relativity and the concept of an equation of state, Phys. Rev. **187,** 1767 (1969).

[11] A. P. Galan, D. Olivieri, and H. Michinel, From optics to dark matter: A review on nonlinear Schrödinger–Poisson systems, Physica (Amsterdam) **403D,** 132301 (2019).

[12] W. Hu, R. Barkana, and A. Gruzinov, Fuzzy Cold Dark Matter: The Wave Properties of Ultralight Particles, Phys. Rev. Lett. **85,** 1158 (2000).

[13] H.-Y. Schive, T. Chiueh, and T. Broadhurst, Cosmic structure as the quantum interference of a coherent dark wave, Nat. Phys. **10,** 496 (2014).

[14] J. S. Bullock and M. Boylan-Kolchin, Small-scale challenges to the ΛCDM paradigm, Annu. Rev. Astron. Astrophys. **55,** 343 (2017).

[15] B. Moore, Evidence against dissipation-less dark matter from observations of galaxy haloes, Nature (London) **370,** 629 (1994).

[16] W. J. G. de Blok, The core-cusp problem, Adv. Astron. **2010,** 1 (2010).

[17] P. Mocz, M. Vogelsberger, V. H. Robles, J. Zavala, M. Boylan-Kolchin, A. Fialkov, and L. Hernquist, Galaxy formation with BECDM—I. Turbulence and relaxation of idealized haloes, Mon. Not. R. Astron. Soc. **471,** 4559 (2017).

[18] N. K. Porayko *et al.* (PPTA Collaboration), Parkes pulsar timing array constraints on ultralight scalar-field dark matter, Phys. Rev. D **98,** 102002 (2018).

[19] N. C. Amorisco and A. Loeb, First constraints on fuzzy dark matter from the dynamics of stellar streams in the Milky Way, arXiv:1808.00464.

[20] A. Lidz and L. Hui, The implications of a pre-reionization 21 cm absorption signal for fuzzy dark matter, Phys. Rev. D **98,** 023011 (2018).

[21] J. C. Niemeyer, Small-scale structure of fuzzy and axion-like dark matter, Prog. Part. Nucl. Phys. **113,** 103787 (2020).

[22] L. M. Widrow and N. Kaiser, Using the Schroedinger equation to simulate collisionless matter, Astrophys. J. **416,** L71 (1993).

[23] C. Uhlemann, M. Kopp, and T. Haugg, Schrödinger method as N-body double and UV completion of dust, Phys. Rev. D **90,** 023517 (2014).

[24] M. Kopp, K. Vattis, and C. Skordis, Solving the Vlasov equation in two spatial dimensions with the Schrödinger method, Phys. Rev. D **96,** 123532 (2017).

[25] P. Mocz, L. Lancaster, A. Fialkov, F. Becerra, and P.-H. Chavanis, Schrödinger–Poisson–Vlasov-Poisson correspondence, Phys. Rev. D **97,** 083519 (2018).

[26] A. Eberhardt, A. Banerjee, M. Kopp, and T. Abel, Investigating the use of field solvers for simulating classical systems, Phys. Rev. D **101,** 043011 (2020).

[27] F. S. Guzmán and L. A. Ureña-López, Evolution of the Schrödinger-Newton system for a self-gravitating scalar field, Phys. Rev. D **69,** 124033 (2004).

[28] F. S. Guzman and L. A. Urena-Lopez, Gravitational cooling of self-gravitating Bose condensates, Astrophys. J. **645,** 814 (2006).

[29] B. Schwabe, J. C. Niemeyer, and J. F. Engels, Simulations of solitonic core mergers in ultralight axion dark matter cosmologies, Phys. Rev. D **94,** 043513 (2016).

[30] E. Seidel and W.-M. Suen, Formation of Solitonic Stars Through Gravitational Cooling, Phys. Rev. Lett. **72,** 2516 (1994).

[31] J. F. Navarro, C. S. Frenk, and S. D. M. White, The structure of cold dark matter halos, Astrophys. J. **462,** 563 (1996).

[32] M. Modugno, C. Tozzo, and F. Dalfovo, Role of transverse excitations in the instability of Bose-Einstein condensates moving in optical lattices, Phys. Rev. A **70,** 043625 (2004).

[33] P. H. Chavanis, Growth of perturbations in an expanding universe with Bose-Einstein condensate dark matter, Astron. Astrophys. **537,** A127 (2012).

[34] T.-P. Woo and T. Chiueh, High-resolution simulation on structure formation with extremely light bosonic dark matter, Astrophys. J. **697,** 850 (2009).

[35] X. Li, L. Hui, and G. L. Bryan, Numerical and perturbative computations of the fuzzy dark matter model, Phys. Rev. D **99,** 063509 (2019).

[36] E. Madelung, Quantentheorie in hydrodynamischer Form, Z. Phys. **40,** 322 (1927).

[37] A. N. Kolmogorov, The local structure of turbulence in incompressible viscous fluid for very large Reynolds numbers, Proc. R. Soc. A **434,** 9 (1991).

[38] M. Kobayashi and M. Tsubota, Kolmogorov Spectrum of Superfluid Turbulence: Numerical Analysis of the Gross-Pitaevskii Equation with a Small-Scale Dissipation, Phys. Rev. Lett. **94,** 065302 (2005).

[39] A. W. Baggaley, J. Laurie, and C. F. Barenghi, Vortex-Density Fluctuations, Energy Spectra, and Vortical Regions in Superfluid Turbulence, Phys. Rev. Lett. **109,** 205304 (2012).

[40] T. C. Wallstrom, Inequivalence between the Schrödinger equation and the Madelung hydrodynamic equations, Phys. Rev. A **49**, 1613 (1994).

[41] O. D. Kellogg, *Foundations of Potential Theory* (Springer, Berlin, Heidelberg, 1967).

[42] S. L. Marshall, A periodic Green function for calculation of coloumbic lattice potentials, J. Phys. Condens. Matter **12**, 4575 (2000).

[43] I. S. Gradshteyn and I. M. Ryzhik, *Table of Integrals, Series, and Products* (Elsevier LTD, Oxford, 2014).

[44] M. Garny and T. Konstandin, Gravitational collapse in the Schrödinger-Poisson system, J. Cosmol. Astropart. Phys. 01 (2018) 009.

[45] T. Zimmermann, M. Pietroni, J. Madroñero, L. Amendola, and S. Wimberger, A quantum model for the dynamics of cold dark matter, Condens. Matter **4**, 89 (2019).

[46] M. Garny, T. Konstandin, and H. Rubira, The Schrödinger-Poisson method for large-scale structure, J. Cosmol. Astropart. Phys. 04 (2020) 003.

[47] W. Bao, H. Jian, N. J. Mauser, and Y. Zhang, Dimension reduction of the Schrödinger equation with Coulomb and anisotropic confining potentials, SIAM J. Appl. Math. **73**, 2100 (2013).

[48] I. Bloch, J. Dalibard, and W. Zwerger, Many-body physics with ultracold gases, Rev. Mod. Phys. **80**, 885 (2008).

[49] M. Olshanii, Atomic Scattering in the Presence of an External Confinement and a Gas of Impenetrable Bosons, Phys. Rev. Lett. **81**, 938 (1998).

[50] L. Salasnich, A. Parola, and L. Reatto, Effective wave equations for the dynamics of cigar-shaped and disk-shaped Bose condensates, Phys. Rev. A **65**, 043614 (2002).

[51] S. Wimberger, R. Mannella, O. Morsch, and E. Arimondo, Resonant Nonlinear Quantum Transport for a Periodically Kicked Bose Condensate, Phys. Rev. Lett. **94**, 130404 (2005).

[52] S. Wimberger, R. Mannella, O. Morsch, E. Arimondo, A. R. Kolovsky, and A. Buchleitner, Nonlinearity-induced destruction of resonant tunneling in the Wannier-Stark problem, Phys. Rev. A **72**, 063610 (2005).

[53] D. B. Owen, M. Abramowitz, and I. A. Stegun, Handbook of mathematical functions with formulas, graphs, and mathematical tables, Technometrics **7**, 78 (1965).

[54] W. Bao and Q. Du, Computing the ground state solution of Bose–Einstein condensates by a normalized gradient flow, SIAM J. Sci. Comput. **25**, 1674 (2004).

[55] W. Bao, I.-L. Chern, and F. Y. Lim, Efficient and spectrally accurate numerical methods for computing ground and first excited states in Bose–Einstein condensates, J. Comput. Phys. **219**, 836 (2006).

[56] P. Choquard, J. Stubbe, and M. Vuffray, Stationary solutions of the Schrödinger-Newton model—An ODE approach, Differ. Integral Equations **21**, 665 (2008).

[57] T. Pang, *An Introduction to Computational Physics* (Cambridge University Press, Cambridge, England, 2006).

[58] P. G. Drazin, *Solitons: An Introduction* (Cambridge University Press, Cambridge, England, New York, 1989).

[59] D. Lynden-Bell, Statistical mechanics of violent relaxation in stellar systems, Mon. Not. R. Astron. Soc. **136**, 101 (1967).

[60] J. Binney, Discreteness effects in cosmological N-body simulations, Mon. Not. R. Astron. Soc. **350**, 939 (2004).

[61] E. Weislinger and G. Olivier, The classical and quantum mechanical virial theorem, International J. Quantum Chem. **8**, 389 (2009).

[62] J. G. Esteve, F. Falceto, and P. R. Giri, Boundary contributions to the hypervirial theorem, Phys. Rev. A **85**, 022104 (2012).

[63] A. Wehrl, On the relation between classical and quantum-mechanical entropy, Rep. Math. Phys. **16**, 353 (1979).

[64] X. Antoine, W. Bao, and C. Besse, Computational methods for the dynamics of the nonlinear Schrödinger/Gross-Pitaevskii equations, Comput. Phys. Commun. **184**, 2621 (2013).

[65] J. Zhang, H. Liu, and M.-C. Chu, Cosmological simulation for fuzzy dark matter model, Front. Astron. Space Sci. **5**, 48 (2019).

[66] F. C. S. Blanes, *A Concise Introduction to Geometric Numerical Integration* (Apple Academic Press Inc., Palm Bay, FL, 2016).

[67] S. Dodelson, *Modern Cosmology* (Elsevier LTD, Oxford, 2003).

[68] A. Lewis, A. Challinor, and A. Lasenby, Efficient computation of CMB anisotropies in closed FRW models, Astrophys. J. **538**, 473 (2000).

[69] S.-F. Chen and M. Pietroni, Asymptotic expansions for large scale structure, J. Cosmol. Astropart. Phys. 06 (2020) 033.

[70] M. Pietroni, Structure formation beyond shell-crossing: Nonperturbative expansions and late-time attractors, J. Cosmol. Astropart. Phys. 06 (2018) 028.

[71] J. Einasto, On the construction of a composite model for the Galaxy and on the determination of the system of Galactic parameters, Tr. Astrofiz. Inst. Alma-Ata **5**, 87 (1965).

[72] A. E. Schulz, W. Dehnen, G. Jungman, and S. Tremaine, Gravitational collapse in one dimension, Mon. Not. R. Astron. Soc. **431**, 49 (2013).

[73] X. Dong, A short note on simplified pseudospectral methods for computing ground state and dynamics of spherically symmetric Schrödinger-Poisson-Slater system, J. Comput. Phys. **230**, 7917 (2011).

[74] V. Zakharov, A. Pushkarev, V. Shvets, and V. Yankov, Soliton turbulence, JETP Lett. **48**, 79 (1988).

[75] R. Jordan and C. Josserand, Self-organization in nonlinear wave turbulence, Phys. Rev. E **61**, 1527 (2000).

[76] P. Maddaloni, M. Modugno, C. Fort, F. Minardi, and M. Inguscio, Collective Oscillations of Two Colliding Bose-Einstein Condensates, Phys. Rev. Lett. **85**, 2413 (2000).

[77] M. Tabor, *Chaos and Integrability in Nonlinear Dynamics* (John Wiley & Sons, New York, 1989).

[78] M. Lakshmanan and S. Rajaseekar, *Nonlinear Dynamics: Integrability, Chaos and Patterns* (Springer Verlag, Heidelberg, 2003).

[79] P. Jain, S. Weinfurtner, M. Visser, and C. W. Gardiner, Analogue model of a FRW universe in Bose-Einstein condensates: Application of the classical field method, Phys. Rev. A **76**, 033616 (2007).

[80] F. Girelli, S. Liberati, and L. Sindoni, Gravitational dynamics in Bose Einstein condensates, Phys. Rev. D **78**, 084013 (2008).

[81] D. Proment, S. Nazarenko, and M. Onorato, Quantum turbulence cascades in the Gross-Pitaevskii model, Phys. Rev. A **80**, 051603 (2009).

[82] T. Lahaye, C. Menotti, L. Santos, M. Lewenstein, and T. Pfau, The physics of dipolar bosonic quantum gases, Rep. Prog. Phys. **72**, 126401 (2009).

[83] R. Plestid, P. Mahon, and D. H. J. O'Dell, Violent relaxation in quantum fluids with long-range interactions, Phys. Rev. E **98**, 012112 (2018).

[84] M. Combescot, R. Combescot, and F. Dubin, Bose–Einstein condensation and indirect excitons: A review, Rep. Prog. Phys. **80**, 066501 (2017).

[85] L. Berezhiani and J. Khoury, Emergent long-range interactions in Bose-Einstein condensates, Phys. Rev. D **99**, 076003 (2019).